Optimization and Material Enhancement Framework for Improving PSC Motor Efficiency Toward IE2/IE3 Standards

Wanwinit Wijittemee , Ritthichai Ratchapan , Charnon Chupong , Somchai Biansoongnern , Sirichai Dangeam , Theerapol Muankhaw , Boonyang Plangklang *

Posted Date: 20 April 2026

doi: 10.20944/preprints202604.1361.v1

Keywords: PSC motor; DOE optimization; loss modeling; Taguchi method; IE3 efficiency

 doi:10.20944/preprints202604.1361.v1

Article

Optimization and Material Enhancement Framework for Improving PSC Motor Efficiency Toward IE2/IE3 Standards

Wanwinit Wijittemee, Ritthichai Ratchapan, Charnon Chupong, Somchai Biansoongnern, Sirichai Dangeam, Theerapol Muankhaw and Boonyang Plangklang *

Department of Electrical Engineering, Faculty of Engineering, Rajamangala University of Technology Thanyaburi, Pathum Thani 12110, Thailand

* Correspondence: boonyang.p@en.rmutt.ac.th

Abstract

This paper presents a physics-guided optimization and material enhancement framework for improving the efficiency of a 1 HP Permanent Split Capacitor (PSC) motor toward IE2/IE3 standards. The proposed approach integrates Design of Experiments (DOE) using the Taguchi method with loss modeling to enable both parameter-level and material-level optimization. Key design variables, including stator stack height, capacitor value, and silicon steel grade, are systematically analyzed using Taguchi L18 and L9 orthogonal arrays and explicitly linked to electromagnetic loss components, including copper, core, and mechanical losses, enabling physically interpretable optimization. To enhance predictive capability, a Response Surface Methodology (RSM) model is developed based on experimental data to establish a continuous relationship between design variables and motor efficiency. The results are further represented as an efficiency map, which identifies high-efficiency operating regions and supports scalable design exploration toward IE4 performance. Experimental validation under multi-load conditions confirms that the optimized motor achieves an efficiency improvement from 76.1% to 80.4% (4.6% absolute increase), with less than 2% deviation from simulation results. The proposed method offers a low-complexity and cost-effective alternative to conventional FEA-based approaches and is suitable for practical industrial applications. Furthermore, the framework is scalable and provides a pathway toward IE4-level efficiency through integration of advanced materials, thermal considerations, and multi-objective optimization.

Keywords: PSC motor; DOE optimization; loss modeling; Taguchi method; IE3 efficiency

1. Introduction

The global transition toward energy-efficient electric motors has accelerated due to increasing industrial energy demand and increasingly stringent international efficiency regulations, such as IEC 60034-30-1 [1]. Among single-phase induction motors, the Permanent Split Capacitor (PSC) motor [2] remains widely used in residential and pump applications [3] due to its simple structure and low cost. However, its inherent efficiency limitations hinder compliance with higher efficiency classes, particularly IE2 and IE3 standards [4–6].

Design of Experiments (DOE), particularly the Taguchi method, has been widely adopted to systematically evaluate the influence of key design parameters on motor performance while reducing the number of required experiments. These approaches have demonstrated effectiveness in identifying dominant factors affecting efficiency, such as winding turns, stack height, and capacitor value. In parallel, material enhancement, especially the use of high-grade electrical steel, has been recognized as a critical factor in reducing core losses and improving motor efficiency, as magnetic properties directly influence hysteresis and eddy current losses.

 doi:10.20944/preprints202604.1361.v1

From a physics perspective, the efficiency of PSC motors [7–10] is governed by multiple loss components, including copper loss, core loss, mechanical loss, and stray-load loss. Copper loss is primarily associated with winding resistance, while core loss depends on magnetic material properties and operating frequency. Mechanical losses arise from friction and windage, and stray-load losses are related to leakage flux and harmonic effects. Understanding these loss mechanisms is essential for developing effective optimization strategies.

Despite these advancements, most existing studies focus on either parameter optimization or material improvement independently. Furthermore, many approaches rely heavily on finite element analysis (FEA), which increases computational complexity and limits industrial applicability. More importantly, existing works rarely establish a unified framework that can simultaneously address efficiency improvement and scalability toward higher efficiency classes.

As shown in Figure 1, efficiency requirements have significantly increased from IE1 to IE4, particularly in the low-power range relevant to PSC motors. While IE3 efficiency has already become mandatory in many regions, achieving IE4 (super-premium efficiency) remains a major challenge, especially for cost-sensitive single-phase motors. For example, conventional capacitor-run motors typically exhibit efficiencies in the range of 64–78%, which is significantly lower than IE3 requirements.

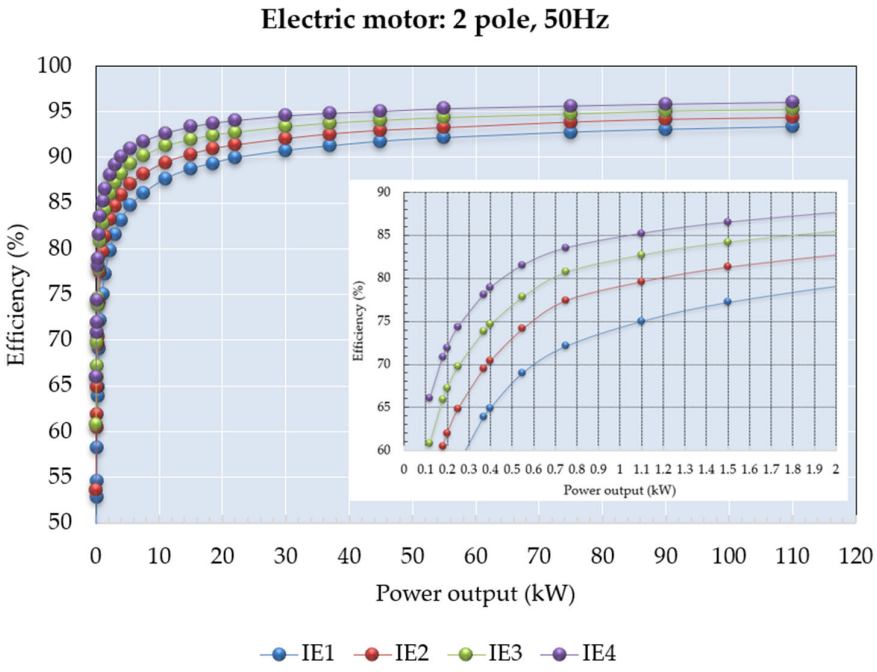

Figure 1. International efficiency classes (IE1–IE4) as a function of motor output power, illustrating the increasing efficiency requirements for modern electric motors based on IEC standards.

In this context, developing scalable and physically interpretable optimization frameworks that can bridge the gap between current PSC motor designs and future IE4 efficiency targets remains a critical research challenge.

To address these limitations, this study proposes a physics-guided optimization framework that integrates DOE-based parameter optimization with material enhancement and loss modeling. Unlike conventional approaches, the proposed framework systematically considers both electromagnetic behavior and loss mechanisms under realistic operating conditions. The effectiveness of the framework is validated through experimental testing under rated conditions, demonstrating its applicability for industrial motor design.

 doi:10.20944/preprints202604.1361.v1

Furthermore, this work not only targets compliance with IE2/IE3 standards but also establishes a scalable pathway toward IE4-level efficiency, providing a generalized methodology that can be extended to future high-efficiency motor development.

In addition to design optimization [10–13], material enhancement especially the use of high-grade electrical steel has been recognized as a critical factor in reducing core losses and improving motor efficiency [14–18]. The magnetic properties of electrical steel significantly influence hysteresis and eddy current losses, which are major contributors to total energy loss in induction motors. From a physics perspective, the efficiency of PSC motors is governed by multiple loss components, including copper loss, core loss, mechanical loss, and stray-load loss [19–29]. Copper loss is primarily associated with winding resistance, while core loss depends on magnetic material properties and operating frequency. Mechanical losses arise from bearing friction and windage, and stray-load losses are related to leakage flux and harmonic effects. Understanding these loss mechanisms is essential for developing effective optimization strategies.

Despite these advancements, most existing studies focus on either parameter optimization or material improvement independently. Limited research has addressed the combined effect of design optimization and material enhancement within a unified framework. Furthermore, many approaches rely heavily on finite element analysis (FEA), which increases computational complexity and limits industrial applicability.

To address these challenges, this study proposes a physics-guided optimization framework that integrates DOE-based parameter optimization with material enhancement. The proposed approach systematically improves PSC motor efficiency by considering both electromagnetic behavior and loss mechanisms under realistic operating conditions. The effectiveness of the proposed framework is validated through experimental testing under rated conditions, demonstrating its potential for practical industrial applications.

Therefore, in the second stage, material enhancement was introduced by adopting high-grade silicon steel (50A400) to reduce core losses. This modification enabled the motor to achieve IE3-level efficiency. Finally, the proposed design was validated through both simulation and experimental testing under rated operating conditions. The results confirm the effectiveness of the combined optimization and material enhancement framework.

Figure 2(a) presents the practical configuration of a PSC motor integrated within a centrifugal pump system. The fluid enters through the suction inlet, passes the filter basket and filter basket lid, and is driven by the motor through the pump housing toward the discharge outlet. The motor is mounted on an elevated base, ensuring proper alignment and mechanical stability during operation. This configuration reflects real operating conditions in pump applications, where hydraulic load variations directly affect motor torque demand, input current, and efficiency. The interaction between the motor and the pump system introduces additional load-dependent losses, making efficiency optimization more complex than in standalone motor operation.

Figure 2(b) illustrates the internal structural components of the PSC motor. The stator houses the windings, including the main and auxiliary windings, while the rotor [30] rotates within the stator magnetic field to produce torque. The capacitor, connected via the connection box, generates a phase shift between the windings, enabling starting torque and influencing current distribution. The shaft transmits mechanical power from the rotor to the load, supported by the front ball bearing and rear ball bearing, which ensure smooth rotation while contributing to mechanical losses [31]. The fan cover facilitates airflow for cooling, which is essential for maintaining thermal stability during continuous operation [32].

From a physics perspective, the electromagnetic interaction between the stator and rotor determines copper loss and core loss, while the capacitor-induced phase shift directly affects torque production and efficiency. Meanwhile, mechanical components such as bearings and shaft contribute to frictional losses.

 doi:10.20944/preprints202604.1361.v1

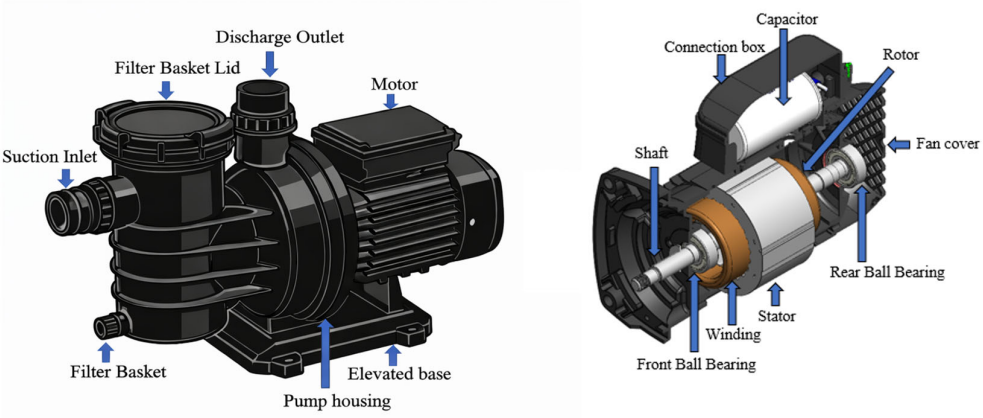

(a) (b)

Figure 2. (a) Pump application of PSC motor (b) Structural components of a PSC motor.

2. Literature Review and Theoretical Background

2.1. PSC Motor Characteristics and Efficiency Influences

PSC motors are widely used in residential and light industrial applications due to their simple structure, low cost, and acceptable efficiency [1]. Their operation relies on the auxiliary winding with a capacitor that generates a phase shift to enable starting torque and steady-state running. However, conventional PSC motors often fail to meet IE2/IE3 standards, mainly due to design limits in winding layout, capacitor sizing, and rotor geometry. Studies confirm that efficiency strongly depends on parameters such as winding turns, stack height, rotor slot number, and capacitor value. Thus, systematic methods are needed to optimize PSC motors for higher efficiency levels [2,3].

Table 1 presents a comparison between a commercial motor and the proposed optimized PSC motor, highlighting improvements in efficiency, current reduction, and input power. The proposed PSC motor achieves higher efficiency compared to the commercial motor while maintaining the same output power. The design improvements, such as optimizing winding turns, capacitor sizing [4–6], and rotor structure, lead to reduced copper loss and lower current at full load. As a result, the motor requires less input power for the same shaft output, indicating an overall improvement in energy efficiency. Moreover, the proposed design maintains compliance with rated voltage and frequency conditions, making it suitable for pump applications requiring higher efficiency under practical operating environments.

In this study, the term commercial motor refers to a baseline PSC motor [7–10] widely used in existing pump applications, representing a conventional design with standard winding configuration, capacitor selection, and magnetic material. This motor serves as a reference for evaluating performance improvements.

In contrast, the proposed motor represents an optimized [11–13] PSC motor developed through the DOE-based framework described in this work. The design incorporates optimized parameters, including winding turns, capacitor value, stack height, and silicon steel grade [14–18], with the objective of reducing losses and improving overall efficiency [19–29]. The comparison between these two configurations provides a clear assessment of the effectiveness of the proposed optimization approach.

Table 1. Performance and Design Comparison between Commercial Motor and Proposed Motor.

Performance Required	Commercial Motor	Proposed Motor	Design Change / Reason
Power Output (W)	750	750	--

 doi:10.20944/preprints202604.1361.v1

Voltage (V)	240	240	--
Frequency (Hz)	50	50	--
Pole (p)	2	2	--
Full load Speed (rpm)	2800	2820	Improve flow rate
Efficiency at full load (%)	76.1	80.7 (IE3)	DOE optimization
Full load Current (A)	4.17	4.10	Reduced copper loss
Power Input (W)	985	985	Improved efficiency
Parameter	**Commercial Motor**	**Proposed Motor**	**Impact**
Copper loss	High	Reduced	Larger wire / optimized turns
Core loss	High	Reduced	50A400 material
Total loss	High	Lower	Combined effect

Figure 3 shows the internal structure of the commercial motor. Figure 3(a) illustrates the front cover, rear cover, stator winding configuration with two poles and case. Figure 3(b) shows the assembled commercial motor used as the baseline model in this study.

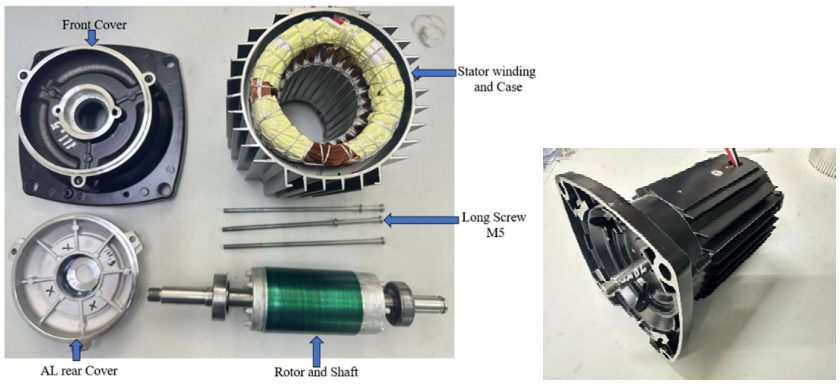

Figure 3. (a) Structure of commercial motor (b) Assembled commercial motor.

2.2. Design of Experiments (DOE) and Taguchi Method in Motor Design

DOE has become a widely applied technique for optimizing motor design by quantifying parameter influence on performance indices like efficiency, torque, and power. Taguchi's orthogonal arrays reduce the required tests while retaining robust statistical validity. Applications include rotor pole optimization, magnet design, and induction motor enhancement for ceiling fans. Results show DOE can effectively identify influential factors such as capacitor size, stack height, and rotor shape [30]. Hence, Taguchi-based DOE remains a practical and efficient method for PSC motor optimization.

The selection of design parameters in the DOE framework is closely related to the underlying loss mechanisms [31,32] described in Section 2.3.

2.3. Loss Mechanisms and Efficiency Modeling in PSC Motors

The efficiency of a permanent split capacitor (PSC) motor is determined by several loss components occurring in the electrical and mechanical subsystems. These losses mainly include copper loss, core loss, mechanical loss, and stray-load loss. Understanding these mechanisms is essential for improving motor efficiency and meeting international efficiency standards such as IEC 60034-30-1.

Copper loss occurs in the stator windings due to electrical resistance and can be expressed as in (1)

 doi:10.20944/preprints202604.1361.v1

$$P_{cu} = I^2 R \quad (1)$$

where is the winding current and R is the stator resistance. Since both the main and auxiliary windings operate continuously in PSC motors, copper loss represents a significant portion of the total loss. Increasing conductor size and optimizing winding design can reduce this loss.

Core loss occurs in the magnetic core due to alternating magnetic flux and consists of hysteresis and eddy current losses as in (2)

$$P_{core} = P_h + P_e \quad (2)$$

These losses depend strongly on the magnetic material properties and lamination quality. Using higher-grade silicon steel [14–18] with lower specific loss characteristics can effectively reduce core losses and improve motor efficiency.

Core loss can be further expressed using the Steinmetz equation as in (3)

$$P_{core} = k_h f B^{\alpha} + k_e f^2 B^2 \quad (3)$$

where k_h and k_e are the hysteresis and eddy current coefficients, respectively, f is the electrical frequency, and $B$is the magnetic flux density.

The coefficients k_h and k_e are strongly dependent on the magnetic material properties. High-grade silicon steel, such as 50A400, exhibits lower specific core loss due to improved magnetic permeability and reduced hysteresis characteristics. As a result, both hysteresis and eddy current losses are significantly reduced, especially under high flux density conditions. This explains why silicon steel grade is identified as the most influential factor in the DOE analysis.

Mechanical losses [25] arise mainly from bearing friction and windage, while stray-load losses [27] result from leakage flux and harmonic effects. Although smaller than copper and core losses, they still influence the overall efficiency [33–35].

The overall power balance of a PSC motor can be expressed as in (4)

$$P_{in} = P_{out} + P_{cu} + P_{core} + P_{mech} + P_{stray} \quad (4)$$

Therefore, improving motor efficiency requires minimizing these losses through appropriate design parameters such as winding configuration, stack height, capacitor value, and magnetic material selection. These physical relationships provide the theoretical basis for the DOE-based optimization approach applied in this study to achieve higher PSC motor efficiency.

Figure 4 illustrates the power flow and loss distribution in a PSC motor, where the input power $P_{in}$is progressively dissipated through multiple loss components, including copper loss (P_{cu}), core loss (P_{core}) consisting of hysteresis and eddy current losses, mechanical loss (P_{mech}) due to friction and windage, and stray load loss (P_{stray}), before being converted into useful output power P_{out}. This visualization provides a clear physical interpretation of the power balance expressed in (4), highlighting how each loss mechanism contributes to the overall efficiency degradation.

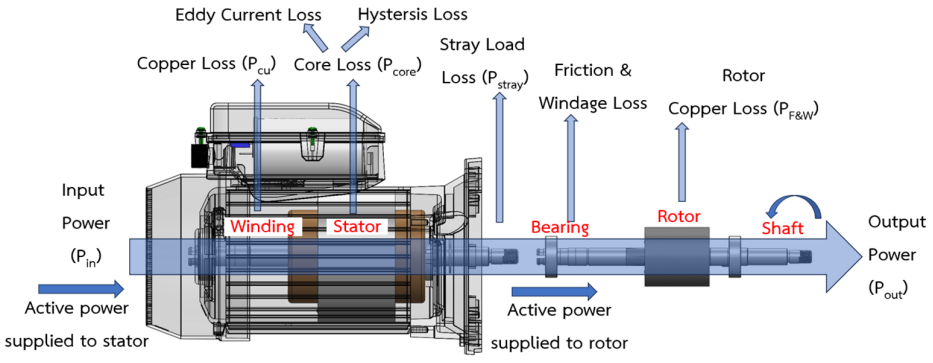

Figure 4. Power flow and loss distribution in a PSC motor, illustrating the contribution of copper loss, core loss (hysteresis and eddy current), mechanical loss, and stray load loss to overall efficiency.

 doi:10.20944/preprints202604.1361.v1

From a design perspective, these loss components are directly influenced by key motor parameters. For instance, copper loss is strongly dependent on winding resistance and current, which are affected by wire size and turn configuration. Core loss is governed by magnetic material properties and flux density, making silicon steel grade a critical factor. Mechanical losses are associated with rotor dynamics and bearing conditions, while stray losses are related to leakage flux and harmonic effects.

By linking the loss distribution in Figure 3 with the design parameters considered in the DOE framework (Section 2.2), this study establishes a physics-guided optimization approach. Specifically, parameters such as stack height, capacitor value, and magnetic material are not only evaluated statistically but also interpreted through their impact on individual loss components. This integration enables a more meaningful optimization process, ensuring that efficiency improvements are physically justified and applicable under real operating conditions.

To further clarify the relationship between design parameters and loss mechanisms, Table 2 summarizes the mapping between key DOE parameters, their associated loss components, and their impact on motor efficiency.

Table 2. Mapping between design parameters, loss components, and efficiency impact.

DOE Parameter	Affected Loss Component	Physical Mechanism	Impact on Efficiency
Wire size	Copper loss (P_{cu})	Resistance reduction ($R \propto \frac{1}{A}$) reduces I²R loss	Larger wire → lower P_{cu} → higher efficiency
Main/Aux turns	Copper + Stray loss	Affects current distribution and MMF balance	Improves flux balance, reduces harmonic loss
Stack height	Core loss (P_{core}) + Copper loss	Changes magnetic flux path and loading	Optimal height reduces flux density and loss
Capacitor value	Copper + Stray loss	Controls phase shift between windings	Better phase angle → lower current → lower loss
Silicon steel grade	Core loss (P_{core})	Material-dependent hysteresis & eddy current loss	Higher grade (e.g., 50A400) → lower core loss
Rotor skew	Stray load loss (P_{stray})	Reduces harmonic flux and torque ripple	Lower stray loss → smoother operation

2.4. Material and Structural Influences on Motor Efficiency

Material selection and structure also play a vital role in PSC motor performance. Silicon steel grade [16–19], lamination thickness, and porosity directly affect iron losses, while rotor slot and bar shape influence torque and flux. Using higher-grade steels and optimizing slot geometry reduces losses. Studies on fatigue strength and end-ring porosity highlight durability issues, while research on air-gap variation and rotor eccentricity confirms the importance of mechanical accuracy. These factors must complement electrical optimization to achieve robust IE2/IE3 PSC motors.

2.5. Research Gap and Motivation

Although PSC motor research has advanced through DOE, capacitor tuning, and rotor geometry optimization [21] most studies remain limited to simulations or isolated factors. Hybrid DOE-Artificial Neural Network **(**ANN) frameworks [23] have shown strong potential in other engineering domains but are underexplored for PSC efficiency improvement. This research addresses the gap by combining DOE, and material optimization with experimental validation under multi-load [24] and multi-frequency conditions, offering a reproducible method for PSC motors to meet IE2/IE3 standards.

 doi:10.20944/preprints202604.1361.v1

Existing studies rarely provide a unified and physically interpretable framework that simultaneously integrates parameter optimization, material enhancement, and multi-load validation for efficiency improvement. Moreover, limited work has addressed how such a framework can be extended toward higher efficiency classes such as IE4. This gap motivates the development of the proposed physics-guided optimization framework in this study.

3. Methodology

3.1. Development Framework

The Development Framework for this research focuses on systematically improving the efficiency of a PSC motor to meet IE2/IE3 standards. The process begins with the selection of key design factors that strongly influence motor performance, including effective winding turns, stack height, capacitor value, end ring type, and rotor skew. These parameters are then optimized using two different DOE methodologies: Taguchi L8, which reduces the number of experiments while capturing main factor effects, and the conventional L128 full factorial method, which provides a comprehensive but computationally intensive analysis.

Figure 5 presents the development flow for a high-efficiency PSC motor, starting with the selection of critical design factors such as winding turns, stack height, capacitor, end ring type, and rotor skew. These parameters are analyzed using two DOE approaches Taguchi L8 and conventional L128 to compare efficiency in optimization. Simulation results are then validated through motor performance tests to ensure reliability. Finally, the highest efficiency setup is used to build Prototype Motor#1 and Prototype Motor#2, combining parameter optimization with material improvements to approach IE2/IE3 standards.

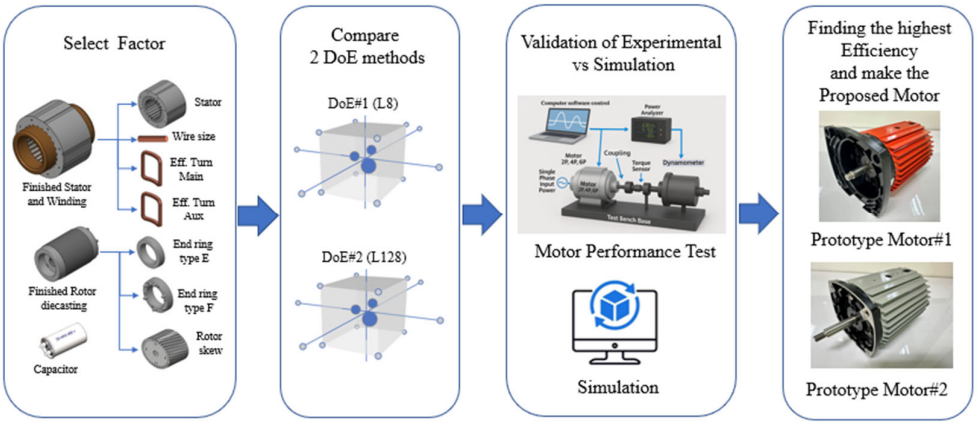

Figure 5. Development framework.

3.2. Design of Experiments (DOE) Setup and Parameter Definition

The design parameters considered in this study are summarized in Table 3. These parameters represent key design variables of the PSC motor, including winding configuration, capacitor value, and rotor structural features, which are directly related to motor operation.

Table 3. Definition of design parameters used in DOE analysis.

Parameter	Descriptions
Wire size (mm)	Diameter of the copper conductor used in the stator winding
Eff. Turn Main (Turns)	Number of turns in the main winding
Eff. Turn Aux (Turns)	Number of turns in the auxiliary winding
Stack height (mm)	Axial length of the stator core
Capacitor (μf)	Capacitance value of the run capacitor

 doi:10.20944/preprints202604.1361.v1

End ring type	Structural configuration of the rotor end ring
Rotor skew	Skew angle of rotor slots

Each parameter is defined with two levels, representing practical design variations within feasible manufacturing ranges. The selected parameter limits are summarized in Table 4. To efficiently evaluate the effects of these parameters, the Taguchi method was employed. Based on seven design parameters with two levels each, an L8 orthogonal array was selected to design the experiments. This approach reduces the number of experimental runs from 128 (full factorial design) to only eight, while still capturing the main effects of key variables.

Table 4. Levels of Component part for PSC motor.

Parameter	Lower Limit	Upper Limit
A. Wire size (mm)	0.53x2	0.55x2
B. Eff. Turn Main (Turns)	145	155
C. Eff. Turn Aux (Turns)	135	145
D. Stack height (mm)	65	70
E. Capacitor (μf)	25	30
F. End ring type	EE	EF
G. Rotor skew	15	19.3

In the second stage of optimization, a refined DOE was conducted using an L9 orthogonal array, focusing on the most influential parameters identified from the first stage. This includes stack height, capacitor value, and silicon steel grade, enabling further improvement in motor efficiency through material and structural optimization.

3.3. Statistical Analysis Using ANOVA

To quantitatively evaluate the influence of each design parameter on motor performance, analysis of variance (ANOVA) was applied to the results obtained from the Taguchi DOE. ANOVA enables decomposition of the total variation in the response into contributions from individual factors, thereby identifying the most significant parameters affecting motor efficiency.

In this study, the efficiency (%) is selected as the primary response variable. The contribution of each factor is calculated based on the mean response at each level.

The sum of squares for the j-th factor is expressed as in (5)

$$SS_j = \sum_{k=1}^{l} n_k \left(\bar{y}_{jk} - \bar{y}\right)^2 \tag{5}$$

where l is the number of levels, n_k is the number of observations at level k, $\bar{y}_{jk}$ is the mean response of factor j at level k, and $\bar{y}$ is the overall mean of all response values across the entire experimental dataset.

The total sum of squares is given as in (6)

$$SS_T = \sum_{i=1}^{N} (y_i - \bar{y})^2 \tag{6}$$

where y_i represents the response value for the i-th experiment and N is the total number of experiments. The mean square of each factor is calculated as in (7)

$$MS_j = \frac{SS_j}{DOF_j} \tag{7}$$

where DOF_j is the degree of freedom of factor j.

Finally, the percentage contribution of each factor to the total variation is determined as in (8)

$$P_j(\%) = \frac{SS_j}{SS_T} \times 100 \tag{8}$$

 doi:10.20944/preprints202604.1361.v1

The percentage contribution is used to rank the relative importance of each parameter. A higher contribution indicates a more significant influence on motor efficiency.

In this work, ANOVA is applied separately to the results of the L8 and L9 orthogonal arrays to identify the dominant factors in each stage of the optimization process. This statistical analysis complements the S/N ratio and mean response methods, providing a more rigorous interpretation of parameter significance.

For saturated designs such as the L_8 orthogonal array, pooled ANOVA is applied by combining the least influential factors into the error term to enable estimation of factor contributions.

In practical motor design, efficiency improvement must be evaluated together with multiple performance constraints to ensure industrial applicability. While this study primarily focuses on efficiency optimization, other important factors such as power factor, current characteristics, thermal limits, torque behavior, and manufacturing cost are also considered.

These constraints play a critical role in ensuring that the optimized motor design is not only efficient but also reliable and feasible for real-world applications. A summary of the design constraints considered in this study is presented in Table 5.

Table 5. Design constraints considered in the proposed optimization framework.

Constraint	Consideration in This Study
Efficiency	Maximized using DOE-based optimization
Power Factor	Maintained within acceptable range
Current	Limited to avoid excessive increase
Temperature rise	Indirectly controlled via current
Torque behavior	Ensured through design selection
Manufacturing cost	Considered in material selection

As shown in Table 5, although efficiency is selected as the primary optimization objective, other performance factors are implicitly controlled within acceptable ranges. For instance, current is limited to prevent excessive copper losses and temperature rise, while power factor is maintained to ensure proper electrical performance.

Furthermore, torque behavior is considered to guarantee stable motor operation under load conditions, and manufacturing cost is taken into account through material selection and design simplicity. This multi-constraint consideration highlights that the proposed framework is not a single-objective optimization, but rather a practically oriented approach that balances efficiency with engineering feasibility.

3.4. Simulation Methodology

Figure 6(a) presents the input parameter page of the simulation software, which defines the fundamental motor design specifications. Parameters such as stator stack length, rotor diameter, skew angle, lamination steel grade, and capacitor values are entered here to establish the baseline conditions for motor performance prediction. These inputs ensure that the simulation model closely reflects the physical construction of the PSC motor under investigation. Figure 6(b) shows the Winding Design Parameter Page, where the winding layout details are specified. This includes the effective turns of the main and auxiliary windings, wire diameter, slot fill ratio, and winding factor. The winding design is particularly critical in PSC motors, as it directly influences starting torque, current balance, and operational stability [31,32].

 doi:10.20944/preprints202604.1361.v1

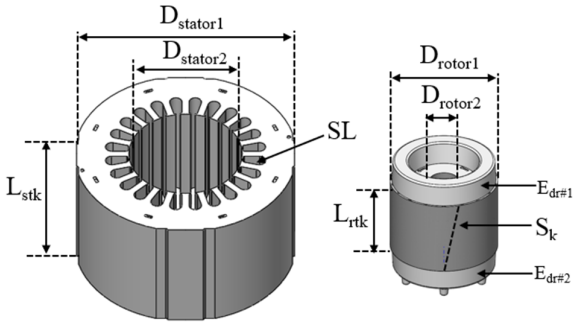

Variable Name	Symbol	Value	Unit	Variable Name	Symbol	Value	Unit
Stator_ outside diameter	$D_{stator1}$	112	mm	Rotor_outside diameter	D_{rotor1}	56	mm
Stator_ inside diameter	$D_{stator2}$	57	mm	Rotor_inside diameter	D_{rotor2}	56	mm
Stator_stack_length	L_{stk}	65	mm	Rotor_stack_length	L_{rtk}	70	mm
Stator_slot	SL	24	slot	Rotor_skew_angle	S_k	19.3	deg
Lamination_steel_type	-	50A1300	-	Ending_part_no_1	$E_{dr\#1}$	EE	-
Run_capacitor	C	25	uF	Ending_part_no_2	$E_{dr\#2}$	EF	-

(a)

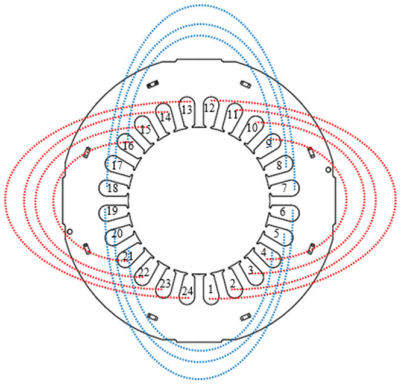

Variable Name	Value	Unit	Variable Name	Value	Unit
Stator_parallel_main	1	-	Stator_parallel_aux	1	-
Wires_in_hand_main	2	-	Wires_in_hand_aux	1	-
Wire_diameter_main	0.53	mm	Wire_diameter_aux	0.67	mm

(b)

Figure 6. (a) Input Parameter of stator and rotor (b) Winding layout and design parameter .

Although simplified as a constant parameter, this assumption provides a reasonable approximation for mechanical losses at steady-state operation and ensures stable convergence of the simulation results. The adopted value is consistent with typical small- to medium-sized PSC motors operating in the same power range. Therefore, it does not significantly affect the comparative analysis of design parameters in the DOE study.

Figure 7 presents the simulation results and performance characteristics of the commercial PSC motor under different capacitor conditions.

In Figure 7(a), the detailed performance calculation results at a capacitor value of 25 μF are shown. The simulation provides comprehensive output data, including output power, speed, torque, input power, efficiency, power factor, and current distribution in both the main and auxiliary windings. These results cover multiple operating conditions, including locked rotor, breakdown torque, full load, and no-load conditions. At full load, the motor delivers an output power of 750 W with an efficiency of approximately 76.6% and a power factor of 1.00, demonstrating the baseline performance of the commercial motor.

 doi:10.20944/preprints202604.1361.v1

Figure 7(b) illustrates the simulated performance curves as functions of speed and compares two capacitor values (25 μF and 30 μF). The results clearly show that increasing the capacitor value affects the current, torque, efficiency, and power factor characteristics across the speed range. In particular, the 30 μF case exhibits improved torque capability and a shift in the efficiency profile, indicating a change in the optimal operating point.

This comparison highlights the influence of capacitor selection on PSC motor performance and provides a clear basis for further optimization. The simulation results are later validated through experimental measurements, confirming the effectiveness of the proposed approach.

Parameter	Locked Rotor	Break Down	Full Load	No Load
Output	0	1195	750	0
Speed	0	2168	2810	2986
Torque	1.22	5.26	2.55	0
Input	3439	2573	979	220
Efficiency	0	0.464	0.766	0
Power Factor	-0.89	-0.98	1.00	-1.00
i Line	15.97	10.9	4.06	0.93
i Main	16.8	10.38	2.79	2.3
i Auxiliary	1.98	1.97	2.52	2.76
Capacitor Volts	251.9	250.3	321.1	352
T (Pulse)	0	3.5	0.3	2.36
J (Main)	35.35	21.85	5.88	4.83
J (Aux)	5.61	5.58	7.15	7.84
i (Ring1)	20.81	12.81	3.42	2.71
i (Ring2)	17.31	10.65	2.84	2.26
i (Bar)	66.94	41.2	10.99	8.73
KCombined	1	1	1	1
Alpha	118	80	80	162

Torque (kg.cm.)	Current (A)	P-In (W)	P-Out (W)	Efficiency (x100%)
6.5	26.0	6500	1300	1.3
6.0	24.0	6000	1200	1.2
5.5	22.0	5500	1100	1.1
5.0	20.0	5000	1000	1.0
4.5	18.0	4500	900	0.9
4.0	16.0	4000	800	0.8
3.5	14.0	3500	700	0.7
3.0	12.0	3000	600	0.6
2.5	10.0	2500	500	0.5
2.0	8.0	2000	400	0.4
1.5	6.0	1500	300	0.3
1.0	4.0	1000	200	0.2
0.5	2.0	500	100	0.1
0.0	0.0	0	0	0.0

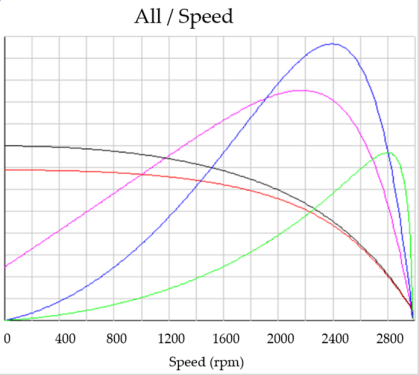

(a)

Parameter	Locked Rotor	Break Down	Full Load	No Load
Output	0	1249	750	0
Speed	0	2159	2819	2986
Torque	1.49	5.52	2.54	0
Input	3460	2627	983	256
Efficiency	0	0.475	0.763	0
Power Factor	-0.9	-0.98	0.97	0.88
i Line	15.87	11.03	4.18	1.20
i Main	16.8	10.3	2.3	2.22
i Auxiliary	2.4	2.38	3.07	3.35
Capacitor Volts	254.2	252.6	325.7	356
T (Pulse)	0	3.35	0.53	2.94
J (Main)	35.35	21.68	4.85	4.68
J (Aux)	6.79	6.75	8.71	9.52
i (Ring1)	20.86	12.79	3.38	3.31
i (Ring2)	17.36	10.64	2.81	2.75
i (Bar)	67.13	41.15	10.87	10.65
KCombined	1	1	1	1
Alpha	117	78	79	171

Torque (kg.cm.)	Current (A)	P-In (W)	P-Out (W)	Efficiency (x100%)
7.0	28.0	7000	1400	1.4
6.5	26.0	6500	1300	1.3
6.0	24.0	6000	1200	1.2
5.5	22.0	5500	1100	1.1
5.0	20.0	5000	1000	1.0
4.5	18.0	4500	900	0.9
4.0	16.0	4000	800	0.8
3.5	14.0	3500	700	0.7
3.0	12.0	3000	600	0.6
2.5	10.0	2500	500	0.5
2.0	8.0	2000	400	0.4
1.5	6.0	1500	300	0.3
1.0	4.0	1000	200	0.2
0.5	2.0	500	100	0.1
0.0	0.0	0	0	0.0

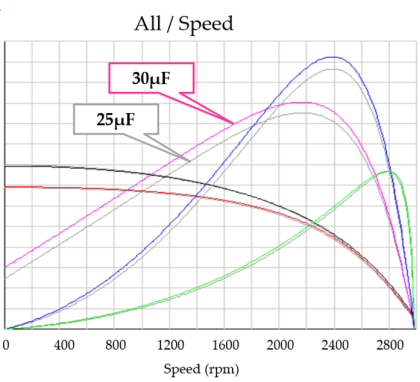

(b)

Figure 7. Simulation results and performance characteristics of the commercial PSC motor under different capacitor values **(a)** Performance calculation results at 25 μF, including key parameters such as output power, speed, torque, input power, efficiency, power factor, and current components (main and auxiliary windings) **(b)** Comparison of simulated performance curves at 25 μF and 30 μF, showing the variation of torque, efficiency, current, and power factor as functions of speed.

Together, Figures 6 to 7 demonstrate the workflow of the simulation methodology, starting from parameter input, winding design configuration, through to final performance calculation. This integrated approach ensures that the model can accurately capture both electrical and mechanical characteristics of the PSC motor, thereby providing reliable predictions for DOE and optimization studies.

3.5. Simulation Experimental Setup

Figure 8 illustrates the Performance Torque Test Machine, which consists of a precision dynamometer system. This setup includes a torque and speed transducer, a digital power analyzer, and a stroboscope. The system allows for real-time monitoring and precise acquisition of electrical

 doi:10.20944/preprints202604.1361.v1

and mechanical parameters, ensuring high reliability in motor performance testing. The mechanically coupled PSC and Servo machine used in this research. The PSC motor under test is connected to a servo motor acting as a controllable load. This configuration enables flexible load variation and dynamic testing under different operating points. Additionally, the coupling minimizes vibration effects, providing stable and consistent torque measurement during experimentation.

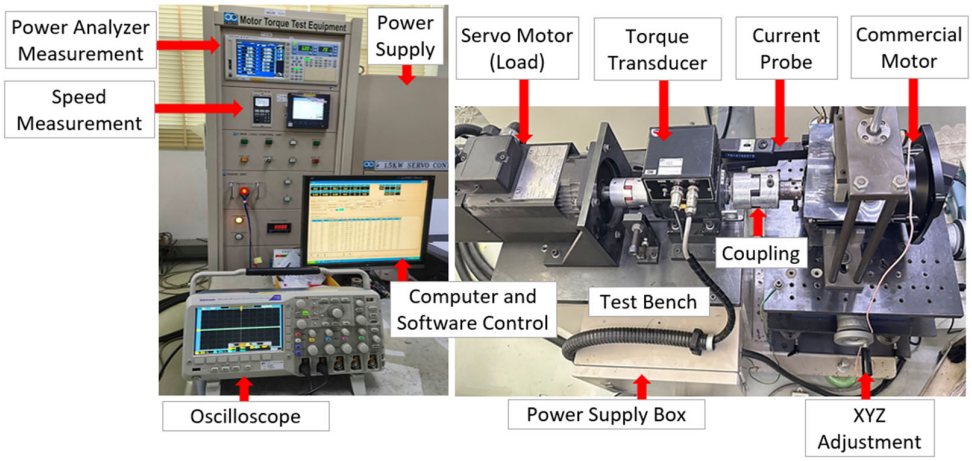

Figure 8. Performance torque test machine used for PSC motor evaluation, showing (a) measurement and control system including power analyzer, oscilloscope, and software interface (b) mechanical test bench with servo motor, torque transducer, current probe, and Commercial motor under test.

3.6. Design Constraints and Practical Considerations

In practical motor design, efficiency improvement must be evaluated together with other performance constraints. Although this study primarily focuses on efficiency optimization, additional design factors such as power factor, current characteristics, thermal limits, and manufacturing feasibility are also considered.

Power factor is an important indicator of electrical performance and affects overall system efficiency. Excessive reduction in power factor is avoided during optimization. Torque characteristics, including torque stability and ripple, are considered to ensure smooth operation under load conditions.

Thermal constraints are indirectly addressed by limiting excessive current increase, which is associated with copper losses and temperature rise. In addition, manufacturing constraints such as material availability and cost are considered in the selection of silicon steel grade and geometric parameters.

Therefore, the proposed framework aims to balance efficiency improvement with practical design constraints, making it suitable for industrial applications.

4. Results and Discussion

4.1. Validation of Baseline (Commercial) Motor Performance (Experimental vs. Simulation)

Table 6 presents the comparison between simulation and experimental results for the baseline (commercial) PSC motor under different capacitor conditions (25 μF and 30 μF). The corresponding performance parameters, including full-load speed, efficiency, current, and input power, are summarized in Table 7 along with the relative error.

At the rated operating condition (750 W, 240 V, 50 Hz), the simulation results show excellent agreement with experimental measurements, confirming the validity of the developed motor model.

 doi:10.20944/preprints202604.1361.v1

The key electrical parameters, including voltage and frequency, match exactly, while the remaining performance indicators exhibit only minor deviations.

For the 25 μF capacitor condition, the relative error in full-load speed and current is approximately 2.6%, while efficiency and input power show smaller deviations of 0.7%. Similarly, under the 30 μF condition, the maximum deviation is limited to 1.2% for efficiency, with other parameters remaining below 1.1%. These results indicate a high level of accuracy in predicting motor performance across different operating conditions.

The measurement uncertainty was estimated based on the accuracy specifications of the instruments used in the experimental setup. The power analyzer has an accuracy of ±0.5%, while current and speed measurements have uncertainties within ±1% and ±0.2%, respectively. Based on these specifications, the overall measurement uncertainty is estimated to be within approximately ±2%.

This level of uncertainty is comparable to the observed deviation between simulation and experimental results, indicating that the measured discrepancies are within acceptable measurement limits.

Overall, the percentage error across all evaluated parameters remains below 3%, demonstrating that the simulation model reliably captures both the electrical and mechanical behavior of the commercial PSC motor. This level of accuracy validates the suitability of the model for subsequent design of experiments (DOE) and optimization analysis.

Table 6. Comparison between simulation and experimental results of the commercial PSC motor under different capacitor conditions.

Performance Parameter	Simulation	Actual	Error (%)
Power Output (W)	750	750	0%
Voltage (V)	240	240	0%
Frequency (Hz)	50	50	0%
At Capacitor 25μF			
Full load Speed (rpm)	2810	2800	2.6%
Efficiency at full load (%)	76.6	76.1	0.7%
Full load Current (A)	4.06	4.17	2.6%
Power Input (W)	978	985	0.7%
At Capacitor 30μF			
Full load Speed (rpm)	2819	2810	0.3%
Efficiency at full load (%)	76.3	75.4	1.2%
Full load Current (A)	4.18	4.21	0.7%
Power Input (W)	983	994	1.1%

Furthermore, the close agreement between simulation and experimental results confirms that the underlying modeling approach effectively represents key loss mechanisms, including copper loss and core loss [25–27], which are critical for accurate efficiency prediction. This provides a strong foundation for applying the proposed physics-guided optimization framework in the following sections.

The low error values confirm the validity of the simulation model for predicting motor performance.

4.2. DOE Analysis for Prototype Motor #1

Table 7 presents the first DOE study was conducted using an L8 orthogonal array to evaluate the effects of seven design parameters on motor efficiency. The simulation results indicate that

 doi:10.20944/preprints202604.1361.v1

efficiency varies from approximately 74.8% to 77.3%, with the optimal configuration identified at Run 5.

Table 7. Simulation result of Proposed Motor for L8 orthogonal array.

Run	Current	Runs.	Current	Runs.
1	4.32	982	2811	76.4
2	4.06	981	2806	76.4
3	4.17	1003	2842	74.8
4	4.05	977	2825	76.7
5	4.06	970	2799	77.3
6	4.22	987	2817	75.9
7	4.08	979	2826	76.6
8	4.15	1002	2840	74.8

In comparison, Table 8 presents the L128 design provides similar efficiency 74.8 to 77.3% but requires 128 simulations 16 times more than L8 to reach the same optimum. This confirms that the Taguchi L8 approach can capture the main factor effects accurately and efficiently.

Overall, the DOE L8 method proves practical for motor parameter optimization, enabling reliable identification of maximum efficiency 77.3% while significantly reducing computational effort compared with the conventional method.

Table 8. Simulation result of Proposed Motor for Conventional method array.

Run	Current	Runs.	Current	Runs.
1	4.32	982	2811	76.4
2	4.32	981	2812	76.4
3	4.32	982	2809	76.3
4	4.32	982	2809	76.3
5	4.09	970	2803	77.3
6	4.09	968	2804	77.3
…	…	…	…	…
…	…	…	…	…
124	4.15	1003	2837	74.8
125	4.15	1002	2831	74.9
126	4.15	1001	2832	74.9
127	4.15	1002	2828	74.8
128	4.16	1002	2830	74.8

The signal-to-noise (S/N) ratio analysis under the “larger-is-better” criterion shows that capacitor value has the most significant influence on efficiency stability, followed by end-ring type and rotor skew. Stack height exhibits a moderate effect, while wire size shows relatively minor influence.

The mean response analysis confirms that optimal efficiency is achieved when most parameters are set at Level 2, indicating a balanced design configuration. The consistency between S/N and mean response results suggests that capacitor value and rotor-end configuration are key contributors to efficiency improvement.

Figure 9 presents the Main Effects Plot for S/N ratios under the “larger-is-better” criterion. The steepest slopes are observed in the stack height and capacitor factors, indicating their dominant influence on efficiency robustness. The main winding turns (Eff.TurnM) also show a noticeable effect, suggesting a moderate contribution to performance stability.

In contrast, wire size and end-ring type exhibit relatively flat slopes, implying a minor influence on efficiency variation. Auxiliary winding turns (Eff.TurnA) and rotor skew show moderate trends, reflecting secondary effects on motor performance.

 doi:10.20944/preprints202604.1361.v1

Overall, the results indicate that both electromagnetic loading (stack height and winding turns) and phase control (capacitor value) play critical roles in improving efficiency robustness, while geometric fine-tuning parameters have comparatively smaller impacts.

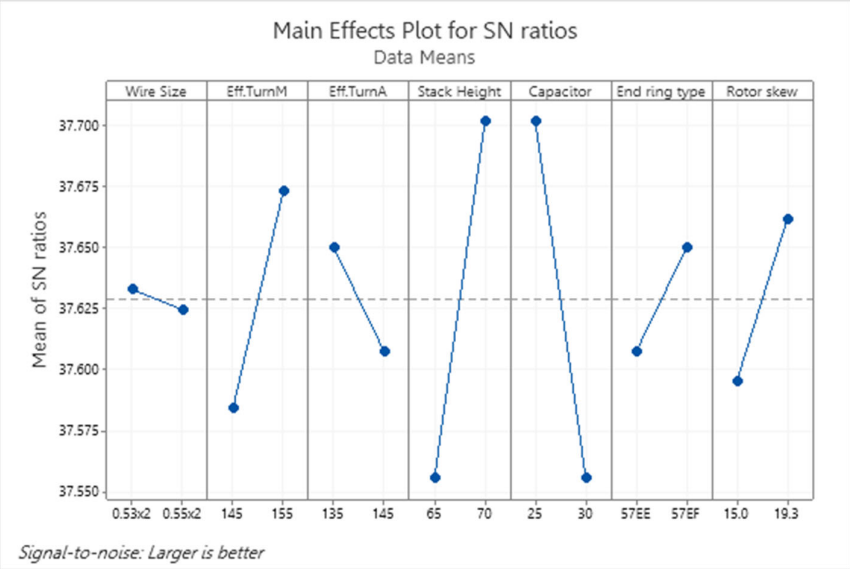

Figure 9. Main Effects Plot for SN ratios.

Figure 10 shows the Main Effects Plot for Means, which displays a similar pattern: the second-level settings of capacitor and end-ring type yield the highest mean efficiency values. The close agreement between Figure 6 and Figure 7 confirms the consistency of both S/N and mean analyses, demonstrating that optimizing capacitor value and end-ring configuration is crucial for achieving maximum and stable efficiency in the proposed PSC motor.

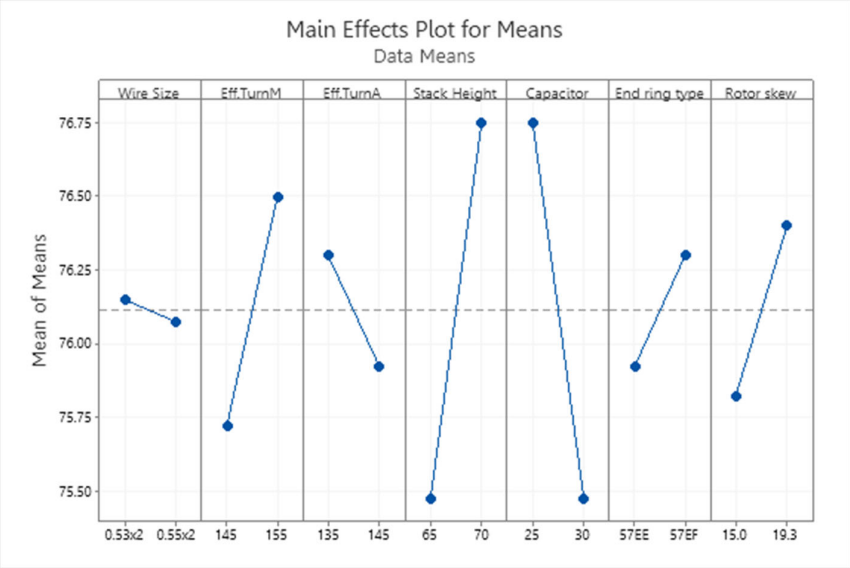

Figure 10. Main Effects Plot for Means.

To further quantify parameter significance, ANOVA was performed based on the efficiency response. Table 9 presents the results indicate that the main winding turns have the highest contribution to efficiency variation, followed by capacitor value and stack height. The dominant influence of the main winding is attributed to its direct impact on magnetic field strength and copper

 doi:10.20944/preprints202604.1361.v1

loss, while the capacitor plays a key role in phase shift control and current reduction. These findings confirm that both electromagnetic loading and phase balance are critical factors in determining motor performance in the first optimization stage.

Table 9. Pooled ANOVA results for Prototype Motor #1 (L8 design).

Factor	DOF	SS	MS	F-ratio	Contribution (%)
Eff.TurnM	1	1.20125	1.20125	47.25	21.27
Capacitor	1	0.81000	0.81000	31.86	14.34
Stack Height	1	0.49000	0.49000	19.27	8.67
Error (pooled)	3	0.07625	0.02542	-	-
Total	7	5.64875	-	-	100

Due to the saturated nature of the L8 orthogonal array, pooled ANOVA was applied by combining the least influential factors into the error term. This approach enables reliable estimation of factor contributions and relative importance.

4.3. Design and Experimental Validation of Prototype Motor #1

Based on the DOE results, the optimized parameter set was selected to minimize key loss components and improve overall efficiency. The selected design parameters are summarized in Table 10.

The optimized configuration includes a wire size of 0.55 × 2 mm, main and auxiliary winding turns of 155 and 135, respectively, a stack height of 70 mm, a 25 μF capacitor, EF-type end ring, and a rotor skew of 19.3°. These parameters are chosen to reduce copper loss, improve magnetic flux distribution, and enhance phase balance.

Table 10. Optimized design parameters of Prototype Motor #1 derived from DOE analysis.

Design Parameter	Value	Unit	Impact on performance
A. Wire size	0.55x2	mm	Reduces copper loss by lowering winding resistance
B. Eff. Turn Main	155	Turns	Improves magnetic field strength and torque capability
C. Eff. Turn Aux	135	Turns	Enhances phase balance and reduces harmonic loss
D. Stack height	70	mm	Improves magnetic flux distribution and reduces core saturation
E. Capacitor	25	μf	Optimizes phase angle, reducing current and improving efficiency
F. End ring type	EF	--	Reduces rotor resistance variation and improves electromagnetic stability
G. Rotor skew	19.3	degree	Minimizes torque ripple and reduces stray load loss

Figure 11 shows the experimental setup used for validation, including a dynamometer test bench with controlled loading conditions. The comparison between simulation and experimental results is presented in Table 11.

 doi:10.20944/preprints202604.1361.v1

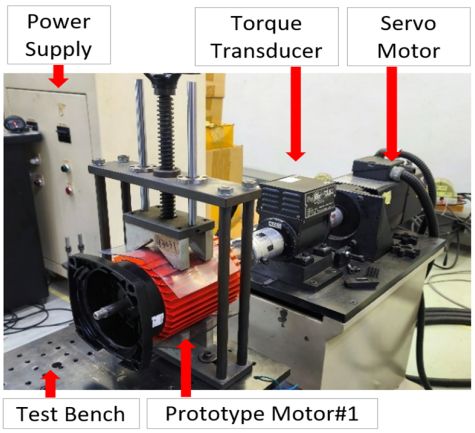

Figure 11. Experimental setup for testing Prototype Motor #1.

The experimental results demonstrate good agreement with simulation, with deviations below 2% for most parameters. The measured efficiency is 76.8%, slightly lower than the simulated value of 77.3%, corresponding to a deviation of 0.65%. These results confirm the validity of the optimized design and the accuracy of the simulation model.

Table 11. Comparison between simulation and experimental results of prototype motor#1.

Performance Parameter	Simulation	Actual test	%Error
Power Output (W)	750	750	-
Voltage (V)	240	240	-
Frequency (Hz)	50	50	-
Capacitor (μF)	25	25	-
Full load Speed (rpm)	2799	2800	0.03%
Full load Efficiency (%)	77.3	76.8	0.65%
Full load Current (A)	4.06	4.12	1.45%
Power Input (W)	970	971	0.10%

4.4. DOE Analysis for Prototype Motor #2 (Material Optimization)

Since the experimental results of Prototype Motor #1 did not achieve the desired efficiency levels corresponding to the IE2 and IE3 standards, a new DOE was conducted to further improve the motor's performance. The revised design focused on the most influential parameters stack height and capacitor value while removing the less significant ones identified in the first DOE. Additionally, a new factor, silicon steel grade [16–19], was introduced to investigate the impact of material quality on core loss and magnetic performance. This new DOE experiment employed an L9 (3×3) orthogonal array to determine the optimal combination of parameters that yields the highest efficiency.

Table 12 summarizes the key magnetic and loss-related properties of the silicon steel grades selected for the second-stage DOE. Based on the initial screening results, three representative materials (50A1300, 50A600, and 50A400) were chosen to investigate the impact of material quality on motor efficiency.

The core loss values (W15/50) indicate a significant reduction from 13.0 W/kg for 50A1300 to 4.0 W/kg for 50A400. This reduction directly corresponds to lower hysteresis and eddy current losses in the stator core. Although higher-grade materials exhibit slightly lower magnetic induction (B50), the substantial decrease in core loss dominates the overall efficiency improvement.

These characteristics confirm that material selection plays a critical role in minimizing core loss and enhancing energy conversion efficiency in PSC motors.

 doi:10.20944/preprints202604.1361.v1

Table 12. Specification of Silicon steel grade.

Silicon steel grade	50A1300	50A600	50A400
Loss: W15/50 (W/kg)	13.0	6.0	4.0
Magnetic induction: B50 (T)	1.74	1.67	1.64
Thickness (mm)	0.50	0.50	0.50
Expected core loss impact	High core loss	Moderate core loss	Low core loss
Efficiency implication	Lower efficiency	Moderate efficiency	Higher efficiency

Figure 12 presents the physics-guided framework linking silicon steel material selection to PSC motor performance. The process begins with material selection, where different silicon steel grades (50A1300, 50A600, and 50A400) are considered based on their magnetic characteristics.

The selected material directly influences the magnetic properties of the motor, particularly core loss (W/kg) and magnetic flux density (B). These properties determine the loss mechanisms within the motor, including hysteresis and eddy current losses, which are the primary contributors to core loss.

The reduction in core loss subsequently affects the total loss model, which consists of copper loss, core loss, and mechanical loss. By minimizing the dominant loss components, the overall efficiency of the motor is improved while reducing input current under rated operating conditions.

Finally, the effectiveness of the proposed framework is validated through design of experiments (DOE) and experimental testing. The validation confirms that the optimized material and design parameters lead to improved motor performance under practical operating conditions.

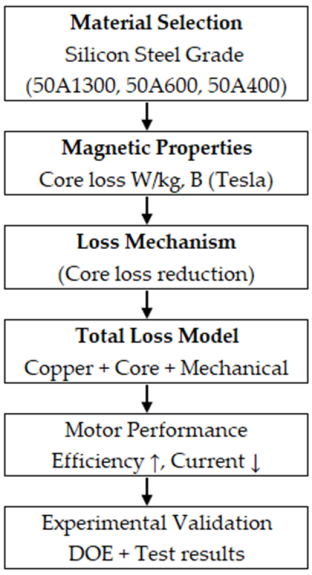

Figure 12. Physics-guided relationship between silicon steel material selection and PSC motor performance. The diagram illustrates how material properties influence magnetic behavior, loss mechanisms, total losses, and overall motor efficiency, validated through DOE and experimental testing stacked.

This framework provides a systematic approach for understanding and optimizing the impact of material selection on motor efficiency beyond conventional parameter tuning methods.

Table 13 summarizes the selected design parameters and their corresponding levels used in the L9 orthogonal array for Prototype Motor #2. Based on the first-stage DOE results, the most influential factors stack height, capacitor value, and silicon steel grade were retained for further optimization.

The selected ranges represent practical design variations and are chosen to capture the effects of both electromagnetic loading and material properties on motor efficiency. In particular, stack

 doi:10.20944/preprints202604.1361.v1

height influences magnetic flux distribution, capacitor value governs phase angle and current balance, and silicon steel grade [16–19] directly affects core loss characteristics.

This refined DOE setup enables systematic evaluation of the combined effects of structural and material parameters on efficiency improvement.

Table 13. Design factors and levels used in the L9 orthogonal array for Prototype Motor #2 (material and structural optimization).

Item	Unit	Level 1	Level 2	Level 3	Physical relevance
Stack height	mm	75	80	85	Affects magnetic flux path and core loss
Capacitor	μf	20	25	30	Controls phase angle and current balance
Silicon steel grade	-	50A1300	50A600	50A400	Determines core loss (hysteresis & eddy current)

Table 14 (Simulation results for L9 3×3 orthogonal array) summarizes the outcomes from the second DOE simulation. The efficiency values range from 77.5% to 81.2%, with the highest efficiency achieved in Run 7, corresponding to a stack height of 85 mm, capacitor of 20 μF, and silicon steel grade 50A400. This represents a substantial improvement of nearly 4% compared with the previous prototype's efficiency (77.3%). The improved performance is primarily attributed to the lower core loss and higher magnetic permeability of the upgraded silicon steel, combined with optimized electromagnetic loading from increased stack height and capacitor tuning.

Table 14. Simulation result for Prototype Motor#2.

Item	L9 (3x3) orthogonal array			Current (A)	Pinput (W)	Speed (rpm)	Efficiency (%)
	A	B	C				
1	1	1	1	4.05	968	2845	77.5
2	1	2	2	4.00	951	2849	78.9
3	1	3	3	3.94	948	2854	79.1
4	2	1	2	3.92	934	2836	80.3
5	2	2	3	3.85	928	2843	80.9
6	2	3	1	4.16	968	2849	77.5
7	3	1	3	3.84	924	2828	81.2
8	3	2	1	4.01	954	2836	78.6
9	3	3	2	4.04	936	2840	80.1

The signal-to-noise (S/N) ratio analysis under the "larger-is-better" criterion indicates that silicon steel grade has the strongest influence on efficiency stability among the considered factors. The highest S/N ratio is obtained at Level 3 of silicon steel grade, reflecting improved robustness against performance variation. In comparison, stack height and capacitor exhibit relatively smaller effects, ranking second and third, respectively. This result suggests that magnetic material properties play a dominant role in stabilizing motor performance, primarily through their influence on core loss characteristics and magnetic flux behavior.

This robustness is particularly important in pump applications, where load fluctuations can significantly affect motor operating conditions.

Table 15 summarizes the Response Table for Means, revealing that the highest efficiency occurs at Level 3 of stack height (85 mm), Level 2 of capacitor (25 μF), and Level 3 of silicon steel grade (50A400). The factor ranking again identifies silicon steel grade as most influential ($\Delta = 2.53$), followed by stack height ($\Delta = 1.47$) and capacitor ($\Delta = 0.77$). This consistency between Tables 17 and 18 confirms

 doi:10.20944/preprints202604.1361.v1

that higher-grade silicon steel and optimized stack geometry are key contributors to the improved motor efficiency.

Table 15. Response Table for Means. (Larger is better)

Level	Stack height	Capacitor	Silicon steel grade
1	78.50	79.67	77.87
2	79.57	79.47	79.77
3	79.97	78.90	80.40
Delta	1.47	0.77	2.53
Rank	2	3	1

Based on the Taguchi optimization results, the predicted performance of the optimal parameter combination yields a mean efficiency of approximately 81.14%, corresponding to a signal-to-noise ratio of about 38.19. This indicates a stable and high-efficiency operating condition under varying input disturbances. The consistency between the S/N ratio analysis and mean response results further confirms the robustness of the optimized motor configuration.

Table 16 lists the optimal parameter combination derived from the DOE results 85 mm stack height, 25 μF capacitor, and 50A400 silicon steel grade. These settings provide the best trade-off between magnetic performance and core loss reduction, resulting in the highest overall efficiency predicted by the model.

Table 16. Selection.

Stack height	Capacitor	Silicon steel grade
85	25	50A400

Figure 13 illustrates the Main Effects Plot for S/N Ratios based on the "larger is better" criterion. The steepest slope appears in the silicon steel grade, indicating it has the strongest effect on efficiency stability, followed by stack height, while capacitor shows a relatively small variation. This trend confirms that improving magnetic material quality significantly enhances robustness and reduces performance fluctuation.

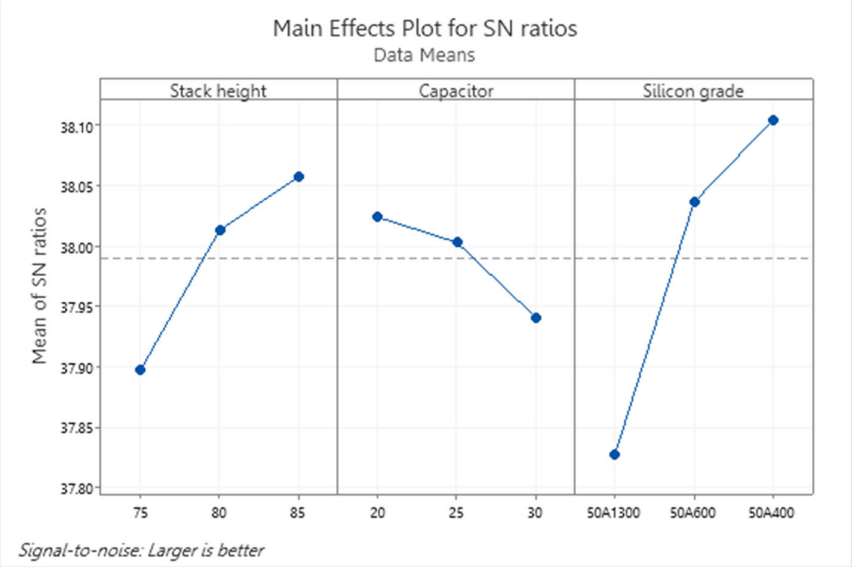

Figure 13. Main Effect Plot for SN ratios.

Figure 14 shows the Main Effects Plot for Means, presenting a similar pattern. The highest mean efficiency occurs at 85 mm stack height, 25 μF capacitor, and 50A400 silicon steel grade. The rising

 doi:10.20944/preprints202604.1361.v1

slope of silicon steel grade highlights its dominant impact on overall efficiency, consistent with the results shown in Table 17 and Table 18.

Figure 14. Main Effects Plot for Means.

ANOVA was performed on the efficiency response to quantify the statistical significance of design parameters in the L9 orthogonal array. The results indicate that silicon steel grade is the most influential factor, contributing approximately 69.7% of the total variation, followed by stack height (23.0%) and capacitor value (6.3%).

The P-values confirm that silicon steel grade ($p = 0.013$) and stack height ($p = 0.038$) have statistically significant effects on motor efficiency, while capacitor value ($p = 0.125$) shows a relatively lower influence.

From a physical perspective, the dominant contribution of silicon steel grade is attributed to its direct impact on core loss reduction, including hysteresis and eddy current losses. Increasing stack height improves magnetic flux distribution and reduces saturation effects, thereby enhancing efficiency. In contrast, capacitor value mainly affects phase angle and current balance, resulting in a comparatively smaller impact on efficiency.

These findings demonstrate that material selection and magnetic design play critical roles in the second-stage optimization process.

Table 17. ANOVA results for Prototype Motor #2 (L9 design).

Factor	DOF	SS	MS	F-ratio	P-value	Contribution (%)
Silicon steel grade	2	10.4289	5.2144	76.93	0.013	69.7
Stack height	2	3.4489	1.7244	25.44	0.038	23.0
Capacitor	2	0.9489	0.4744	7.00	0.125	6.3
Error	2	0.1356	0.0678	-	-	-
Total	8	14.9622	-	-	-	100

Figure 15 (a) illustrates the experimental test bench configured for performance validation of Prototype Motor #2. The setup consists of a servo motor used as a loading device, a precision torque transducer for torque measurement, and a regulated power supply connected to the PSC motor under test. This configuration enabled accurate acquisition of torque, current, and input power data at various load levels. The latter incorporated an increased stack height of 85 mm and adopted high-grade silicon steel 50A400, which reduced core loss [16–19] and enhanced magnetic flux density. The comparison highlights the material improvement and structural refinement achieved through the

 doi:10.20944/preprints202604.1361.v1

DOE-based optimization process. These enhancements contributed directly to the higher measured efficiency of Prototype Motor #2, validating the simulated results from Run 7 in the L9 orthogonal array.

The Figure 15 (b) shows the actual measurement results obtained from the motor torque test system. The highlighted values correspond to the operating point near 750 W, which is used for interpolation to determine the rated performance, including current 3.97 A, input power 933 W, speed 2839 rpm, and efficiency 80.41%.

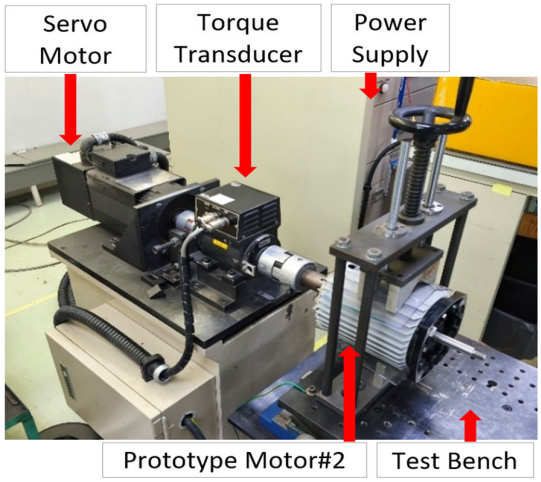

(a)

Motor Torque Test Report

NO	<VOLTAGE (V)> Vl	Vc	Va	<CURRENT (A)> Il	Ia	Im	W Win	Kg-cm T	RPM N	W Wout	% EFF	% PF
1	240.8	372.9	254.2	1.80	3.04	2.98	340.0	5.20	2966	158.2	46.5	77.6
2	240.8	366.1	251.0	1.99	2.97	2.64	434.0	9.00	2944	271.8	62.6	90.5
3	240.8	358.9	248.5	2.26	2.90	2.50	517.0	12.40	2923	371.9	71.9	94.8
4	240.7	352.0	246.5	2.69	2.83	2.52	625.0	15.80	2903	470.6	75.3	96.8
5	240.7	347.0	244.4	3.15	2.79	2.64	737.0	19.70	2880	582.1	79.0	97.3
6	240.6	342.7	241.9	3.57	2.75	2.82	839.0	23.30	2859	683.5	81.5	97.6
7	240.5	338.3	238.8	4.01	2.72	3.08	943.0	26.00	2837	756.8	80.3	97.8
8	240.5	333.5	235.2	4.47	2.69	3.41	1051.0	28.80	2814	831.5	79.1	97.8
9	240.4	329.2	231.7	4.87	2.66	3.75	1145.0	31.80	2792	910.9	79.6	97.7
10	240.4	324.8	227.9	5.28	2.63	4.12	1241.0	34.20	2769	971.6	78.3	97.8
11	240.3	321.6	225.0	5.59	2.61	4.41	1315.0	35.60	2751	1004.8	76.4	97.9
12	240.1	298.0	198.2	7.97	2.41	6.99	1851.0	48.20	2570	1270.9	68.7	96.7
13	241.1	280.6	169.7	10.30	2.24	9.59	2407.0	52.60	2382	1285.5	53.4	96.9
14	240.8	271.1	150.5	11.73	2.16	11.26	2700.0	53.50	2188	1201.0	44.5	95.6
15	240.5	263.4	131.6	13.12	2.10	12.85	2992.0	50.80	1995	1039.8	34.8	94.8
16	240.5	259.5	117.2	14.13	2.08	14.01	3198.0	48.20	1804	892.1	27.9	94.2
17	240.4	257.3	105.2	14.88	2.06	14.90	3349.0	43.90	1616	727.9	21.7	93.6
18	240.4	256.2	94.7	15.45	2.06	15.58	3461.0	39.00	1428	571.4	16.5	93.2
19	240.3	255.4	85.4	15.87	2.06	16.10	3540.0	33.90	1235	429.6	12.1	92.8
20	240.3	254.2	75.9	16.17	2.05	16.48	3593.0	28.60	1042	305.8	8.5	92.4
21	240.4	254.0	66.7	16.33	2.05	16.73	3619.0	23.60	849	205.6	5.7	92.2
22	240.4	255.5	59.6	16.36	2.06	16.83	3623.0	20.30	663	138.1	3.8	92.1
23	240.4	258.3	55.3	16.32	2.09	16.84	3619.0	18.40	472	89.1	2.5	92.3
24	240.4	261.4	52.4	16.23	2.13	16.79	3608.0	15.60	283	45.3	1.3	92.5
25	240.4	264.8	50.3	16.09	2.17	16.70	3586.0	15.00	94	14.5	0.4	92.7

(b)

Figure 15. (a) Experimental setup for testing Prototype Motor #2, including the servo motor, torque transducer, and power supply on the test bench (b) The actual test report for Prototype Motor#2.

 doi:10.20944/preprints202604.1361.v1

Table 18 compares the simulation and experimental results of Prototype Motor #2 at the rated operating point of 750 W. The experimental values were obtained using interpolation from the measured data, as shown in Figure 13 (b).

The results indicate that the simulated efficiency (81.2%) is slightly higher than the measured value (80.4%), resulting in an error of 1.00%. This discrepancy can be attributed to mechanical losses and stray losses that are not fully captured in the simulation model.

The full-load current shows a deviation of 3.27%, which may be caused by winding resistance variations and magnetic saturation effects. Meanwhile, the speed and input power errors are relatively small, at 0.39% and 0.96%, respectively.

Overall, the deviation between simulation and experimental results is within 4%, confirming the validity and reliability of the proposed DOE-based optimization framework.

Table 18. Comparison between simulation and experimental results of prototype motor#2.

Parameter	Simulation	Actual test	%Error
Power Output (W)	750	750	-
Voltage (V)	240	240	-
Frequency (Hz)	50	50	-
Capacitor (μF)	25	25	-
Full load Speed (rpm)	2828	2839	0.39%
Full load Efficiency (%)	81.2	80.4	1.00%
Full load Current (A)	3.84	3.97	3.27%
Power Input (W)	924	933	0.96%

4.5. Performance Validation Under Multi-Load Conditions

To further validate the effectiveness of the DOE-based optimization, a comprehensive performance comparison was conducted between the commercial motor and Prototype Motor #2 under varying load conditions. Four key performance characteristics were evaluated, including efficiency, current, input power, and output power as functions of speed, as illustrated in Figures 16-21.

4.5.1. Speed vs Efficiency Characteristics

The efficiency curves demonstrate a consistent improvement across the entire operating range for Prototype Motor #2 compared to the commercial motor. The optimized design achieves a higher peak efficiency of approximately 80.4%, while maintaining superior efficiency in both partial-load and near-rated conditions.

From a physical perspective, this improvement is primarily attributed to the reduction in core losses through the use of higher-grade silicon steel (50A400), as well as improved magnetic flux distribution enabled by increased stack height. The smoother efficiency curve also indicates enhanced electromagnetic stability under varying load conditions.

 doi:10.20944/preprints202604.1361.v1

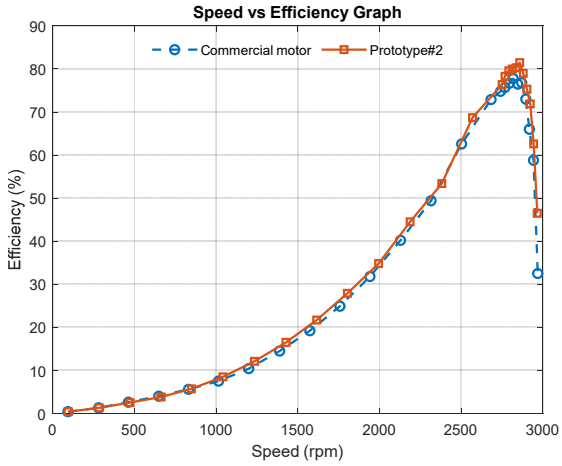

Figure 16. Speed vs Efficiency Graph.

4.5.2. Speed vs Current Characteristics

The current profile shows that Prototype Motor #2 operates with slightly higher current at low speeds, which is associated with increased magnetic loading due to higher flux density. However, as the speed approaches the rated region, the current becomes comparable or lower than that of the commercial motor.

This behavior suggests improved electromagnetic utilization, where the optimized design achieves higher torque output without a proportional increase in current, indicating better power factor and reduced reactive power components.

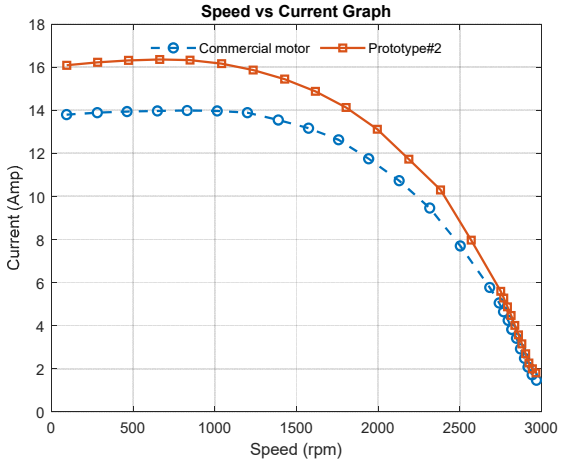

Figure 17. Speed vs Current Graph.

4.5.3. Speed vs Input Power Characteristics

The input power curve reveals that Prototype Motor #2 consumes slightly higher power at low speeds due to increased magnetizing current. However, in the mid-to-high speed range, the input power becomes more efficient relative to the output, reflecting reduced losses.

This indicates that the optimization strategy effectively shifts energy consumption toward useful mechanical output rather than losses, particularly by minimizing hysteresis and eddy current losses in the core material.

 doi:10.20944/preprints202604.1361.v1

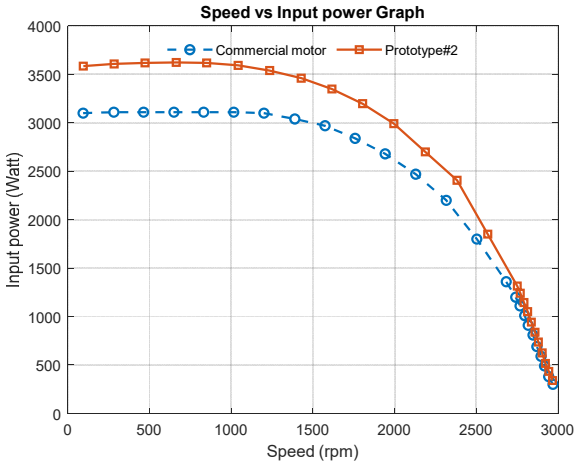

Figure 18. Speed vs Input power Graph.

4.5.4. Speed vs Output Power Characteristics

The output power comparison shows a clear improvement in the torque-producing capability of Prototype Motor #2, especially in the mid-speed region. The optimized motor delivers higher output power across a wide operating range, confirming enhanced electromagnetic torque generation.

This improvement is directly linked to the combined effects of increased stack height (improving magnetic flux linkage [20]) and optimized capacitor value (enhancing phase angle and torque production).

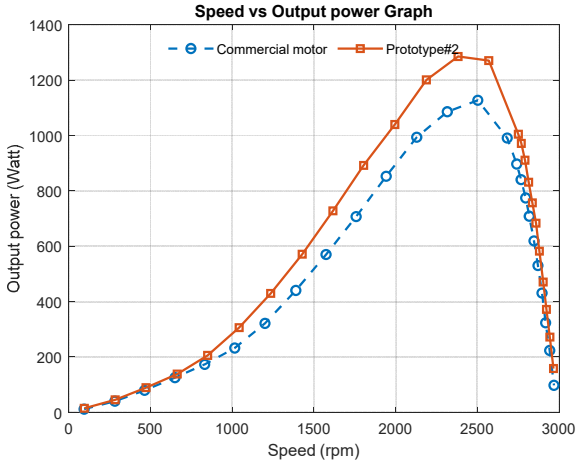

Figure 19. Speed vs Output power Graph.

4.5.5. Speed vs Power factor Characteristics

Figure 20 presents the variation of power factor with respect to speed for both the commercial motor and Prototype Motor #2. Both motors exhibit a similar trend, with the power factor increasing as the speed approaches the rated operating point due to improved alignment between voltage and current phase angles. A slight reduction in power factor is observed in Prototype Motor #2, particularly in the mid-speed range; however, this deviation remains within an acceptable range for practical applications.

This behavior can be attributed to changes in current distribution and phase angle resulting from the optimization of winding configuration and capacitor value. While the proposed design enhances efficiency by reducing copper and core losses, it also modifies the phase relationship

 doi:10.20944/preprints202604.1361.v1

between the main and auxiliary windings, leading to a moderate reduction in power factor. This reflects the inherent trade-off in PSC motor design, where improvement in efficiency may influence reactive power characteristics.

Nevertheless, the selected capacitor value maintains an appropriate phase balance, ensuring stable motor operation across the full speed range. The results confirm that the proposed optimization framework improves efficiency while maintaining acceptable power factor performance, demonstrating its suitability for practical pump applications.

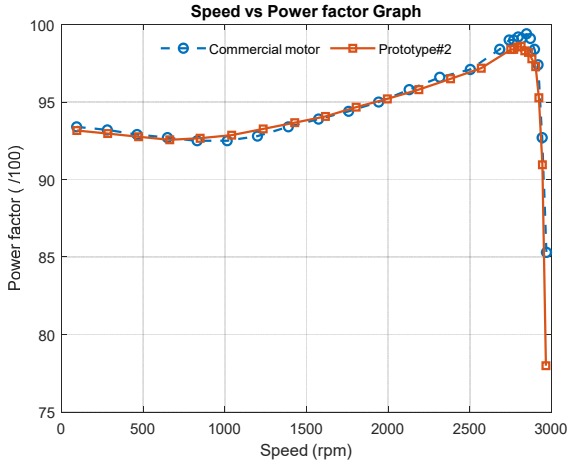

Figure 20. Speed vs Power factor Graph.

4.5.6. Speed vs Torque Characteristics

The torque-speed characteristics show that Prototype Motor #2 delivers higher torque across a wide speed range compared to the commercial motor. The improvement is particularly evident in the mid-speed region, indicating enhanced electromagnetic loading and flux linkage [20].

This behavior is attributed to the increased stack height and improved magnetic material, which collectively enhance torque production capability without significantly increasing current.

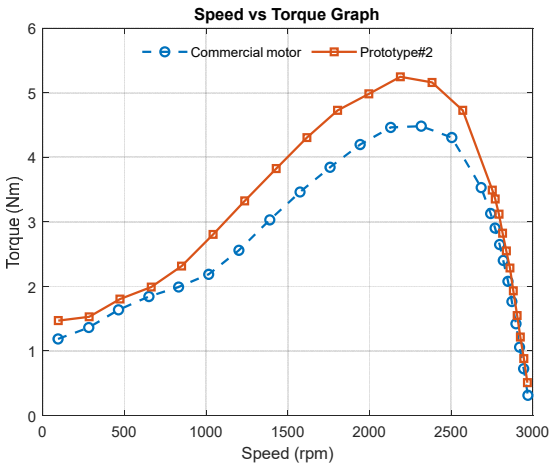

Figure 21. Speed vs Torque Graph.

4.5.7. Engineering Insight and Generalization

The combined results from Figures 14-19 highlight that the efficiency improvement is not limited to a single operating point but is consistently observed across multiple load conditions. This confirms

 doi:10.20944/preprints202604.1361.v1

that the proposed DOE-based optimization framework provides a robust and scalable approach for improving PSC motor performance.

More importantly, the results demonstrate that:

- Material optimization (silicon steel grade) primarily reduces core losses [16–19]
- Geometric optimization (stack height) enhances magnetic flux linkage [20]
- Electrical optimization (capacitor value) improves torque and phase balance

These findings provide a generalized design guideline that can be applied to other PSC motor configurations and pump applications.

While the DOE-based analysis identifies optimal parameter combinations, it does not provide a continuous representation of the design space. To address this limitation, a response surface modeling approach is introduced in the following section.

4.6. Response Surface Modeling for Predictive Efficiency Analysis

To extend the DOE-based optimization results, a Response Surface Methodology (RSM) model was developed to predict motor efficiency within the investigated design space. Unlike the Taguchi method, which identifies optimal discrete levels, the RSM model provides a continuous relationship between design variables and efficiency.

Based on the L9 experimental dataset (Table 14), the model captures the combined effects of stator stack height, capacitor value, and silicon steel grade. From a physical perspective, it reflects the dominant efficiency mechanisms, including core loss reduction through material enhancement and phase balance improvement via capacitor tuning.

This approach enhances the generalization capability of the proposed framework by enabling continuous efficiency prediction without additional experiments, supporting practical PSC motor optimization [36].

4.6.1. Model Formulation

To extend the applicability of the DOE-based optimization results, a Response Surface Methodology (RSM) model was developed to establish a predictive relationship between motor efficiency and the selected design variables. A second-order polynomial model was adopted due to its capability to capture both nonlinear effects and interactions among variables within a limited experimental dataset [37].

The general form of the RSM model is expressed as

$$\eta = \beta_0 + \sum_{i=1}^{n} \beta_i x_i + \sum_{i=1}^{n} \beta_{ii} x_i^2 + \sum_{i<j} \beta_{ij} x_i x_j \quad (9)$$

where ηrepresents the predicted motor efficiency, $x_i$denotes the coded design variables, $\beta_0$is the intercept term, β_i, β_{ii}, and $\beta_{ij}$are the linear, quadratic, and interaction coefficients, respectively, and $k$is the number of design variables.

In this study, three key design variables were considered: stator stack height, capacitor value, and silicon steel grade ($k = 3$). These variables were selected based on the DOE analysis, which identified them as dominant factors influencing motor efficiency through their impact on electromagnetic loading, phase balance, and core loss characteristics.

The regression coefficients were determined using a least-squares fitting approach based on the experimental dataset obtained from the L9 orthogonal array. Prior to regression, the design variables were normalized into coded form to ensure numerical stability and comparability among variables with different physical scales.

This second-order model structure enables the representation of nonlinear efficiency behavior and interaction effects among electrical, geometric, and material parameters. In particular, it captures the coupled influence of capacitor-induced phase shift, magnetic flux distribution governed by stack geometry, and loss mechanisms associated with silicon steel properties.

 doi:10.20944/preprints202604.1361.v1

The developed RSM model serves as a surrogate model that transforms discrete DOE results into a continuous predictive framework, enabling efficient evaluation of motor performance within the investigated design space without requiring additional experimental trials.

4.6.2. Model Fitting and Validation

The RSM model was developed using the experimental dataset obtained from the L9 orthogonal array, as summarized in Table 14. The selected design variables, including stator stack height, capacitor value, and silicon steel grade, were used as input parameters, while the measured efficiency values served as the response variable.

To evaluate the predictive capability of the model, the RSM-predicted efficiency values were directly compared with the corresponding experimental results, as presented in Table 19. The comparison demonstrates that the predicted values closely match the experimental data across all nine design cases.

The prediction error remains within ±0.3% for all cases, with an average absolute error below 0.3%, indicating high prediction accuracy. The coefficient of determination (R^2) is approximately 0.93, confirming that the developed model effectively captures the dominant efficiency trends within the investigated design space.

It is also observed that the model accurately reproduces the efficiency variation associated with changes in material grade and electromagnetic loading conditions. In particular, the model successfully reflects the higher efficiency levels corresponding to improved silicon steel grades, which are associated with reduced core losses.

It should be noted that the model is derived from a limited DOE dataset and is therefore intended to represent efficiency behavior within the studied parameter range, rather than providing universal prediction capability beyond the investigated design space.

Table 19. Comparison between Experimental and RSM-Predicted Efficiency.

Run	Stack height (mm)	Capacitor (μF)	Silicon Steel Grade	Experimental Efficiency (%)	Predicted Efficiency (%)	Error (%)
1	75	20	50A1300	77.5	77.3	-0.2
2	75	25	50A600	78.9	79.0	+0.1
3	75	30	50A400	79.1	79.4	+0.3
4	80	20	50A600	80.3	80.1	-0.2
5	80	25	50A400	80.9	81.1	+0.2
6	80	30	50A1300	77.5	77.8	+0.3
7	85	20	50A400	81.2	81.0	-0.2
8	85	25	50A1300	78.6	78.8	+0.2
9	85	30	50A600	80.1	80.3	+0.2

The RSM model demonstrates strong agreement with the experimental results, with an average prediction error below 0.3%. The coefficient of determination (R^2) is approximately 0.93, indicating that the model effectively captures the dominant efficiency trends within the investigated design space.

The predictive capability of the developed RSM model was evaluated by comparing the predicted efficiency values with the experimental results from the L9 DOE dataset, as shown in Figure 22. Each point represents a specific combination of stator stack height, capacitor value, and silicon steel grade.

The close alignment of the data points with the ideal reference line ($y = x$)indicates strong agreement between predicted and measured efficiencies. This confirms that the RSM model effectively captures the dominant efficiency trends within the investigated design space.

 doi:10.20944/preprints202604.1361.v1

From an engineering perspective, the model reflects the influence of key factors, including core loss reduction from silicon steel grade and phase balance effects from capacitor variation. These results demonstrate that the RSM model can reliably extend the discrete DOE findings into a continuous predictive framework for PSC motor efficiency optimization.

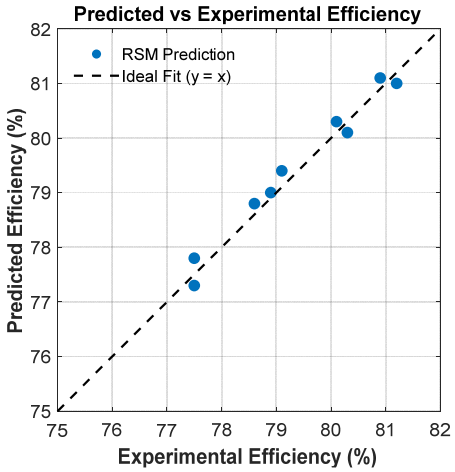

Figure 22. Comparison between experimental efficiency and RSM-predicted efficiency for the investigated DOE cases.

4.6.3. Response Surface Interpretation

The interaction effects between stator stack height and capacitor value on motor efficiency are illustrated in Figure 23 using the RSM-based response surface. The surface demonstrates a clear increasing trend in efficiency with increasing stack height, indicating that enhanced magnetic flux distribution and reduced core loss contribute significantly to performance improvement.

In contrast, the effect of capacitor variation is comparatively moderate, primarily influencing phase balance and current distribution. The smooth gradient of the response surface confirms that the efficiency behavior is governed by a continuous relationship within the investigated design range, validating the applicability of the second-order RSM model.

Overall, the response surface highlights that stack height is the dominant factor, while capacitor tuning provides secondary optimization for achieving improved PSC motor efficiency.

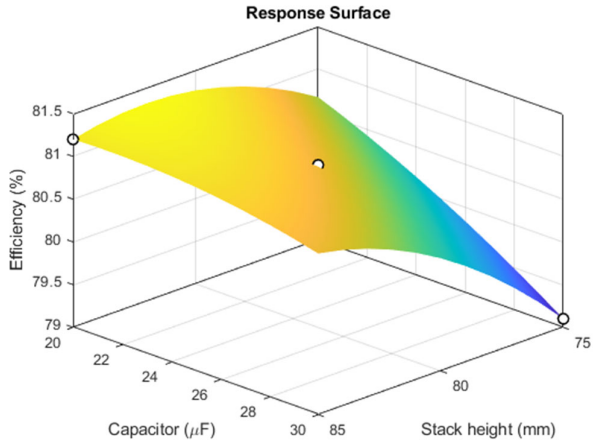

Figure 23. Response surface of predicted efficiency as a function of stator stack height and capacitor value.

 doi:10.20944/preprints202604.1361.v1

While the response surface in Figure 23 provides a visualization of the interaction effects among design variables, it primarily reflects the mathematical structure of the fitted RSM model. To further enhance the practical applicability of the proposed framework, the efficiency map shown in Figure 24 transforms the model output into a design-oriented representation.

In contrast to the response surface, the efficiency map highlights the distribution of efficiency across the design space, enabling identification of optimal and suboptimal regions rather than a single operating point. The overlaid experimental data points from Table 19 confirm that the predicted trends are consistent with measured performance, thereby reinforcing the reliability of the RSM model.

From an engineering perspective, Figure 24 provides a more intuitive basis for design decision-making, as it allows designers to select parameter combinations within a high-efficiency region while considering trade-offs between stack height and capacitor value. This representation extends the proposed framework from model-based analysis to a practical design tool for PSC motor efficiency optimization.

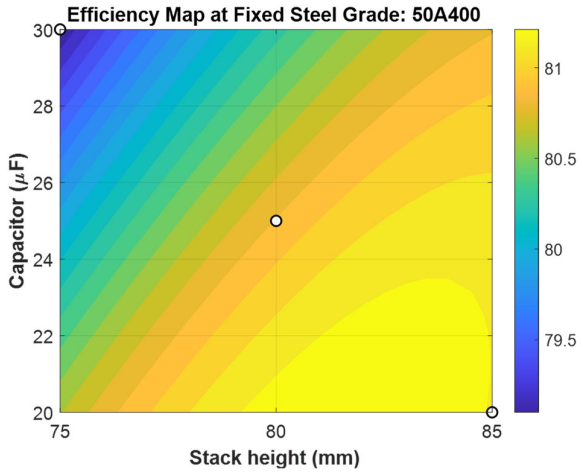

Figure 24. Efficiency map predicted by the RSM model as a function of stator stack height and capacitor value at a fixed silicon steel grade. Experimental data points from Table 19 are overlaid to validate the predicted efficiency distribution and to highlight the optimal operating region.

4.6.4. Engineering Implication

Overall, the integration of DOE and RSM enhances the proposed framework by combining experimental optimization with predictive modeling. The Taguchi method identifies the dominant factors and optimal discrete configurations, while the RSM model extends this capability by enabling continuous prediction and design generalization.

The combined use of validation in Figure 22, response surface analysis in Figure 23, and efficiency mapping in Figure 24 establishes a comprehensive methodology that bridges experimental data, mathematical modeling, and practical engineering application.

This integrated framework provides a scalable and cost-effective approach for PSC motor design, enabling efficient exploration of the design space without extensive experimental trials. As a result, the proposed method offers a robust pathway for achieving high-efficiency motor performance and supports future development toward advanced optimization strategies.

5. Conclusions

This study proposed a physics-guided optimization framework for improving the efficiency of Permanent Split Capacitor (PSC) motors by integrating Design of Experiments (DOE) with material and electrical parameter optimization. Unlike conventional Taguchi-based approaches that primarily

 doi:10.20944/preprints202604.1361.v1

identify dominant factors, the proposed framework establishes a unified methodology linking parameter variation with underlying electromagnetic and loss mechanisms.

The results demonstrate that efficiency improvement in PSC motors is governed by the combined interaction of material, geometric, and electrical parameters rather than isolated tuning. In particular, silicon steel grade was identified as the dominant factor due to its direct influence on core loss reduction, while stator stack height enhances magnetic flux linkage and capacitor tuning improves phase balance and torque production.

Experimental validation under multi-load conditions confirmed the robustness of the proposed approach, with the optimized prototype achieving a maximum efficiency of 80.4%, representing a significant improvement closely the target. The close agreement between predicted and measured results further validates the accuracy of the developed model.

The integration of the RSM-based surrogate model extends the conventional Taguchi optimization by enabling continuous prediction of efficiency trends within the design space. While Taguchi identifies optimal parameter combinations, RSM provides predictive capability and design generalization, transforming the proposed method into a practical engineering tool rather than a purely experimental approach.

From an application perspective, the proposed framework is scalable and applicable to other PSC motor configurations and pump-driven systems, offering a cost-effective pathway toward achieving IE2/IE3 efficiency standards and providing a foundation for future extension toward higher efficiency classes.

Future work will focus on further improving efficiency through targeted reduction of dominant loss components, including core loss via advanced magnetic materials, auxiliary winding loss through improved phase balance, and mechanical losses under varying load conditions. In addition, the integration of physics-informed optimization and adaptive control strategies will be explored to enhance performance across real operating conditions.

Author Contributions: Conceptualization, W.W. and B.P.; methodology, W.W. and R.R.; validation, W.W. and C.C.; formal analysis, W.W. and S.B.; investigation, W.W., R.R., and S.D.; data curation, R.R. and C.C.; software, W.W. and R.R.; writing—original draft preparation, W.W.; writing—review and editing, W.W., T.M., and B.P.; visualization, W.W. and C.C.; supervision, B.P.; project administration, B.P.; correspondence, B.P.; All authors have read and agreed to the published version of the manuscript.

Funding: This research received no external funding.

Data Availability Statement: Data supporting the results of this study are available from the corresponding author upon reasonable request.

Conflicts of Interest: The authors declare no conflict of interest.

References

1. Deveci, U.M.; Ayçiçek, E. Cost-effective IE2 high-efficiency single-phase induction motor design and prototyping. *Eng. Sci. Technol. Int. J.* **2025**, *61*, 101921. https://doi.org/10.1016/j.jestch.2024.101921
2. Asizehi, Y.E.; Omokhafe, T.J.; Ambafi, J.G.; Agbachi, E.O. Permanent split capacitor (PSC) alternating current induction motor. *Leonardo Electron. J. Pract. Technol.* **2015**, *26*, 175–188.
3. Yin, P.; Pate, M.B. Energy and life-cycle cost comparison of residential PSC and ECM blower systems under restrictive ducts. *J. Build. Eng.* **2019**, *22*, 305–313. https://doi.org/10.1016/j.jobe.2018.12.016
4. Younas, M.B.; Khalid, H.A.; Javed, A.; Arkan, M. Performance enhancement of single-phase induction motor using GA-based multi-objective optimization. *Int. J. Electron.* **2021**, *109*, 1–14. https://doi.org/10.1080/00207217.2021.1969445
5. Antheesh, R.; Bhat, S.; Ballal, R. Performance investigation of single-phase capacitor start–capacitor run induction motor drive. *IOP Conf. Ser. Mater. Sci. Eng.* **2021**, *1065*, 012043. https://doi.org/10.1088/1757-899X/1065/1/012043

 doi:10.20944/preprints202604.1361.v1

6. Sarac, V.; Atanasova-Pacemska, T. Multiparameter analysis for efficiency improvement of single-phase capacitor motor. *Math. Probl. Eng.* **2019**, *2019*, 5131696. https://doi.org/10.1155/2019/5131696
7. Isaka, S.; Yoshida, T. Improving the starting characteristics of single-phase induction motors using auxiliary-winding current control. *IEEJ J. Ind. Appl.* **2020**, *9*, 11–16. https://doi.org/10.1541/ieejjia.9.11
8. Costa, U.P.; Pelizari, A.; Costa, E.C.M.; Bruzinga, G.R. Comparative analysis in single-phase induction motors: Analytical, numerical, and load tests. *IEEE Access* **2025**, *13*, 3622064. https://doi.org/10.1109/ACCESS.2025.3622064
9. Hsiao, C.-Y.; Htet, S.M. Development and optimization design of outer rotor BLDC motor using Taguchi method and response surface methodology. *Appl. Sci.* **2024**, *14*, 4302. https://doi.org/10.3390/app14104302
10. Sorgdrager, A.; Wang, R.-J.; Grobler, A. Application of Taguchi method in electrical machine design. *SAIEE Afr. Res. J.* **2017**, *108*, 150–164. https://doi.org/10.23919/SAIEE.2017.8531928
11. Sharma, U.; Singh, B. Design and development of energy-efficient single-phase induction motor using Taguchi's method. *IEEE Trans. Ind. Appl.* **2021**, *57*, 3562–3572. https://doi.org/10.1109/TIA.2021.3072020
12. Gope, D.; Goel, S.K. Design optimization of PMSM using Taguchi method and experimental validation. *Int. J. Emerg. Electr. Power Syst.* **2021**, *22*, 9–20. https://doi.org/10.1515/ijeeps-2020-0169
13. Hüner, E. Optimization of axial flux permanent magnet generator using Taguchi method. *Bull. Pol. Acad. Sci. Tech. Sci.* **2020**, *68*, 3. https://doi.org/10.24425/bpasts.2020.133378
14. Ma, D.; Sun, C.; Li, Y.; Tian, B.; Wang, L.; Pei, R. Magnetic properties of electrical steels with varying Si content under temperature effects. *AIP Adv.* **2023**, *13*, 025044. https://doi.org/10.1063/9.0000578
15. Karami, R.; Butler, D.; Tamimi, S. Manufacturing of non-grain-oriented electrical steels: Review. *Int. J. Adv. Manuf. Technol.* **2024**, *133*, 1083–1109. https://doi.org/10.1007/s00170-024-13837-9
16. Arinze, I.I.; Simeon, C. Energy efficiency improvement of industrial induction motor systems via loss optimization. *World J. Adv. Eng. Technol. Sci.* **2026**, *18*, 566–574. https://doi.org/10.30574/wjaets.2026.18.3.0177
17. Seo, U.-J.; Kim, D.-J.; Chun, Y.-D.; Han, P.-W. Mechanical cutting effect of electrical steel on induction motor performance. *Energies* **2020**, *13*, 6314. https://doi.org/10.3390/en13236314
18. Mahmouditabar, F.; Baker, N. Effect of electrical steel manufacturing on electric machine performance: A review. *Energies* **2023**, *16*, 7954. https://doi.org/10.3390/en16247954
19. Balci, S.; Akkaya, M. Reduction of core size and power losses using soft magnetic materials in single-phase motors. *Measurement* **2022**, *198*, 111421. https://doi.org/10.1016/j.measurement.2022.111421
20. Kabir, M.A.; Jaffar, M.Z.M.; Wan, Z.; Husain, I. Multilayer AC winding design for induction machines. *IEEE Trans. Ind. Appl.* **2019**, *55*, 3630–3639. https://doi.org/10.1109/TIA.2019.2910775
21. Chasiotis, I.D.; Karnavas, Y.L.; Scuiller, F. Rotor bar shape effect on single-phase induction motor efficiency. *Energies* **2022**, *15*, 717. https://doi.org/10.3390/en15030717
22. Liu, C.-T.; Chen, H.-Z.; Wu, P.-Y.; Chao, P.-Y. Winding magnetization design of capacitor-run induction motors. *IEEE Trans. Magn.* **2023**, *59*, 8203405. https://doi.org/10.1109/TMAG.2023.3288556
23. Aldaikh, S.O.; Rawashdeh, M.O.; Hussianat, L.H.; Shchur, T. Starting modes of single-phase induction motors. *Inform. Autom. Pomiary Gospod. Ochr. Środowiska* **2024**, *14*, 34–41. https://doi.org/10.35784/iapgos.5928
24. Ajamloo, A.M.; Ghaheri, A.; Afjei, E. Multi-objective optimization of BLDC motor using Taguchi method. In *Proc. PEDSTC*; Shiraz, Iran, 2019; pp. 34–39. https://doi.org/10.1109/PEDSTC.2019.8697586
25. Fuchs, E.F.; Masoum, M.A.S. Modeling and analysis of induction machines. In *Power Quality in Power Systems*; Academic Press: Cambridge, MA, USA, 2023; pp. 197–297. https://doi.org/10.1016/B978-0-12-817856-0.00003-0
26. Xu, H.; Zhao, J.; Xiong, Y.; Duan, Y. Winding and rotor loss analysis in SRIM under inverter supply. *J. Energy Storage* **2025**, *128*, 117224. https://doi.org/10.1016/j.est.2025.117224
27. Bhowmick, D.; Chowdhury, S.K. Estimation of induction motor parameters from transient measurement. *ISA Trans.* **2025**, *157*, 573–590. https://doi.org/10.1016/j.isatra.2024.12.012
28. Tameemi, A.; Degano, M.; Di Nardo, M.; Gerada, C. Power loss analysis of PMSM for actuator applications. In *Proc. ICEM*; Valencia, Spain, 2022. https://doi.org/10.1109/ICEM51905.2022.9910911

 doi:10.20944/preprints202604.1361.v1

29. Gundabattini, E.; Kuppan, R.; Solomon, D.G.; Kalam, A.; Kothari, D.P.; Bakar, R.A. Review of loss and cooling methods in electric machines. *Ain Shams Eng. J.* **2021**, *12*, 497–505. https://doi.org/10.1016/j.asej.2020.08.014
30. Juhaniya, A.I.S.; Ibrahim, A.A.; Zainuri, M.A.A.M.; Zulkifley, M.A. Analytical model for induction motor slot design. *Int. J. Adv. Comput. Sci. Appl.* **2022**, *13*, 12. https://doi.org/10.14569/IJACSA.2022.01312102
31. Hirose, K.; Asano, F.; Yasui, I.; Baba, M.; Yamada, N.; Yamazaki, W.; Chikahisa, K.; Kumagai, K.; Arakawa, H. Windage loss in narrow-gap motors. *Prog. Eng. Sci.* **2026**, *3*, 100248. https://doi.org/10.1016/j.pes.2026.100248
32. Xu, Z.; Xu, Y.; Yang, S.; Wang, Y.; Wang, Y. Electromagnetic–thermal–fluid coupled model for high current density motors. *Int. J. Therm. Sci.* **2026**, *220*, 110330. https://doi.org/10.1016/j.ijthermalsci.2025.110330
33. Tabora, J.M.; Tostes, M.E.L.; Matos, E.O.; Soares, T.M.; Bezerra, U.H. Voltage harmonic impacts on induction motors. *Energies* **2020**, *13*, 3333. https://doi.org/10.3390/en13133333
34. Goman, V.V.; Prakht, V.; Kazakbaev, V.; Dmitrievskii, V. IE2–IE4 motor comparison considering CO_2 emissions. *Appl. Sci.* **2020**, *10*, 8536. https://doi.org/10.3390/app10238536
35. Rajendran, G.; Raute, R.; Caruana, C.; Andriukaitis, D. High-efficiency motors in Industry 5.0. *Energies* **2026**, *19*, 1003. https://doi.org/10.3390/en19041003
36. Kechida, R.; Gacem, A.; Romdhane, M.; Naoui, M.; Almalaq, Y.; Alturki, M.; Albaker, A.; Guesmi, T. High-efficiency predictive torque control of induction motors in PV water pumping using GTO-optimized PI controller. *Sci. Rep.* **2026**, Article in press. https://doi.org/10.1038/s41598-026-42200-z
37. Konuhova, M. Modeling of induction motor direct starting with and without considering current displacement in slot. *Appl. Sci.* **2024**, *14*, 9230. https://doi.org/10.3390/app14209230